ABSTRACT

Title of Thesis:	INVESTIGATING ALUMINUM NITRIDE AS A PROTECTION LAYER FOR LITHIUM GERMANIUM THIOPHOSPHATE SOLID ELECTROLYTES Sam Klueter, Master of Science, 2022
Thesis Directed By:	Professor Gary Rubloff (Chair, Materials Science And Engineering)

Lithium germanium thiophosphate (LGPS) is an attractive solid-state electrolyte material due to its exceptionally high ionic conductivity, which rivals organic liquid electrolytes. Despite this potential, other properties have impeded its adoption into solid-state batteries, particularly the poor voltage stability of the material at potentials near that of high voltage cathodes or lithium metal. Aluminum nitride (AlN) can serve as an anodic protection interlayer between LGPS and lithium metal, enhancing cell performance. AlN is grown via plasma-enhanced ALD at 250 °C using TMA and both N_2 and NH_3, but the deposited films show significant oxygen contamination originating from the plasma and lack crystallinity. Galvanostatic cycling and electrochemical impedance spectroscopy show that LGPS-coated cells perform better than bare cells, with expected lifetimes >3x greater in certain cases. Finally, XPS line scans highlight the slow room-temperature reactivity between AlN and evaporated lithium, and a computational model is built to aid further XPS experiments.

INVESTIGATING ALUMINUM NITRIDE AS A PROTECTION LAYER FOR LITHIUM GERMANIUM THIOPHOSPHATE SOLID ELECTROLYTES

by

Samuel Klueter

Thesis submitted to the Faculty of the Graduate School of the
University of Maryland, College Park in partial fulfillment
of the requirements for the degree of
Master of Science
2022

Advisory Committee:

Professor Gary Rubloff (Chair, Materials Science And Engineering)

Professor Sang Bok Lee (Chemistry)

Dr. Alexander Kozen (Materials Science And Engineering)

Acknowledgements

I would like to thank my advisor Professor Gary Rubloff, whose support and guidance made research exciting and accessible in an otherwise difficult time. You have helped me adapt to change, persist despite obstacles, and develop a much deeper curiosity. I will forever be a better scientist thanks to you.

I would like to thank Dr. Alex Kozen for his consistent mentorship throughout my time working in the group. No matter what I was working on, I knew I could come to you to discuss my findings and you would happily oblige me, going above and beyond to guide me in my research.

I would like to thank Dr. Davy Stewart for teaching me more than I could ever have hoped to know about vacuum systems, XPS, and many other tools. You always answered my questions – and there were a lot – without ever making them seem stupid.

I would like to thank my colleagues in the group, Dr. Kieth Gregorczyk, Blake Nuwayhid, Haotian Wang, Victoria Ferrari, Kunal Ahuja, and Daniela Fontecha, as well as Professor Sang Bok Lee and the members of his group, for creating a collaborative and positive environment in the lab. I could not have picked a better group of people to work with every day.

I would like to thank my colleagues, roommates, and friends, Stefan Theodoru, John Hoerauf, and Alex Hall, for the countless hours of studying thermodynamics, lengthy discussions of odd materials science questions, and telling me I'm a good cook. I will miss the battery house deeply.

I would like to thank UMDFU for providing me with a sense of community and support throughout my time at UMD, and for always pushing me to improve myself even when it was not easy. I will never forget the memories I have made with you all.

I would like to thank my parents, Jeff Klueter and Tobie Bernstein, and my sister Jessie Klueter, for supporting me and my love for science for as long as I can remember. Through the good times and the bad I could always turn to you, and receive the love and support that I needed. I undoubtedly would not be here today without all that you have done for me. Thank you.

Finally, this research was supported by SK Innovation under research agreement # 19102790. I would also like to thank the Maryland NanoCenter and its AIMLab for their support.

Table of Contents

Part I. Towards High Voltage Solid State Batteries

I.I. Motivation

As the world transitions away from dependence on fossil fuels, many technologies must be developed and implemented to take its place. New energy generation methods, such as solar, wind and nuclear, must be scaled up to replace their fossil fuel counterparts. Grid infrastructure must be modernized to allow for more distributed generation and distribution of power [1]. And, crucially, energy storage technology must continue to advance to meet the fast growing needs of an electrified world. Within the area of energy storage there are a myriad of applications that will require different solutions, from large scale and long duration grid storage, to batteries in mobile and wearable devices, and everywhere in between. So far, however, lithium-ion batteries (LIBs) have dominated most energy storage markets due to their relatively high performance and low cost.

Despite their ubiquity, LIBs do have their downsides. LIBs rely on critical resources such as cobalt, and if the production of batteries is going to continue meeting the growing demand, alternatives must be found [2-5]. LIBs are not cheap enough at present to meet the demands of grid-scale energy storage, where warehouses full of batteries are needed to power entire cities [6,7]. Conventional LIBs also rely on an organic liquid electrolyte, and when the cell is damaged, these liquids can become extremely dangerous. This has become a concern for electric vehicles, where fires are relatively rare but more dangerous and more difficult to extinguish than fires in cars with combustion engines [8]. The problem is not limited to EVs, however. The Samsung Galaxy Note 7, with millions of units sold, had its production halted due to issues resulting in batteries igniting in people's pockets [9]. In order to understand the source of these problems,

and ultimately how to solve them, it's important to understand the fundamentals of how a battery operates.

I.II. Battery Fundamentals

All batteries are composed of three main components: two electrodes, and an electrolyte separating them. When a battery is fully charged, there is an electrochemical potential between the two electrodes, caused by the accumulation of charge carriers in the negative electrode – called the anode. In the case of lithium-ion batteries, those charge carriers are lithium. To reach equilibrium, the lithium must travel through the electrolyte to reach the other electrode – called the cathode – reducing the electric field within the battery and thereby reducing its potential. While these lithium ions can travel through the electrolyte, electrons are blocked due to the electronically insulating nature of the electrolyte. Instead, electrons travel through an external circuit where they can power devices.

The more lithium ions there are in the battery to be shuttled back and forth, the more energy can be stored and released. Additionally, a higher potential difference between the electrodes results in more energy being released per ion, also increasing the capacity of the battery. This means that, generally, a good pair of electrodes should have a very high potential difference and should be able to store a large amount of lithium ions in a given volume and weight.

While batteries have existed for centuries [10], the first rechargeable lithium ion battery was first developed by Stanley Wittingham in 1979, using lithium metal and titanium disulfide as the electrodes [11]. While lithium metal makes a good electrode by the previous two metrics – its potential is as low as can be, and since it is all lithium there is no wasted material – its reactivity

makes it both difficult to manufacture and hazardous. While many different materials have been implemented in batteries since then [12], today most LIBs use graphitic carbon as the anode and nickel manganese cobalt oxide as the cathode. The layered structure of both of these compounds allow for relatively large amounts of lithium to be inserted into the gaps without severe changes to the overall structure. For the electrolyte, conventional LIBs utilize lithium salts dissolved in an organic liquid (or a mixture of organic liquids). Examples of these salts include $LiPF_6$ and $LiClO_4$, and examples of liquids include propylene and ethylene carbonate. In general, these liquids are extremely flammable [13]. While there is work being done to find new materials to improve or replace nearly every component of conventional batteries, efforts to replace organic liquid electrolytes have been focused in part on finding solids to conduct lithium.

I.III. Solid State Batteries

Solid electrolytes have for a long time struggled to compete with liquid electrolytes due to their relatively poor conductivity. In liquids, atoms are highly mobile and disorganized which allows for charged species to migrate easily through them. In contrast, atoms in a solid are relatively fixed in place which means that almost all solids will have extremely poor ionic conductivity. There are, however, exceptions, and finding those exceptions has been a field of ongoing research for the best 50 years.

The first solid lithium conductor developed in 1969 was LiI, but it had a low ionic conductivity between 10^{-7} and 10^{-6} S/cm at room temperature, making it impractical for nearly all uses [14, 15]. Later in 1977, Li_3N single crystals were identified to have ionic conductivities as high as $1.2x10^{-3}$ S/cm, however its low breakdown voltage made it incompatible with most cathode materials [16]. Over the next decades, more and more solid lithium conductors were discovered,

continually pushing up the conductivity to the point where, at present, solid electrolytes can begin to compete with liquid electrolytes [17].

I.IV. LGPS as a Solid Electrolyte

In 2001, Kanno and Murayama published a paper on a new family of inorganic solid electrolytes, dubbed thio-LISICON (for LIthium SuperIonic CONductor) [18]. These crystalline solids come from the Li_2S-GeS_2-P_2S_5 family, with a variety of phases forming as these precursors are mixed in different ratios. For solids of this form, with composition $Li_{4-X}Ge_{1-X}P_XS_4$, the authors report room temperature conductivities as high as 2.2 mS cm^{-1} for crystals with x=0.75 and a negligible electronic contribution. What's more, the authors show that in a Li/LGPS/Au cell, LGPS is stable between -0.5 and 5 V vs. lithium, giving it a very large voltage stability window.

On the backs of this first discovery, Kamaya et al. reported on a similar thioLISICON electrolyte $Li_{10}GP_2S_{12}$ [19]. This material - synthesized by reaction in a quartz tube furnace from the same precursors as the original thio-LISICONs - has a different crystal structure with a tetragonal unit cell (a=8.717 A, c=12.635 A) and space group $P\,4_2\,/\,n\,m\,c$. This new crystalline material reached a room temperature conductivity of 12 mS cm^{-1}, the highest reported for a solid electrolyte at the time, even matching or exceeding some liquid electrolytes. The voltage stability seemed comparable to previous thioLISICONS, and with their LCO/LGPS/In cell achieving a capacity of 120 mAh g^{-1} at 14 mA g^{-1}, it seemed that LGPS could quickly become the gold standard for solid electrolytes.

Part II: Solid-Electrolyte Interphases: Formation and Mitigation

II.I. SEI Formation

One of the main reasons why the discovery of LGPS has not (to this date) taken over the commercial battery industry is the formation of solid-electrolyte interphases (SEIs).

In any battery, ions migrate along the potential gradient during discharge. This is because, when the cathode is placed in contact with a source of lithium, the lithium-free phase is less stable than the lithiated phase. If allowed, the cathode's lithiated phase will form at the expense of the lithium-free phase, which creates a driving force for lithium to be transported across the cell. In much the same way, it's possible that the electrolyte in a battery is not in its most thermodynamically stable phase when in contact with the electrodes. In this case, the electrolyte may react with either the cathode or anode to form new products at the interfaces, resulting in new materials forming which make up the solid-electrolyte interface.

Several models exist to explain SEI formation, as summarized by Cheng et al. [20]. Peled's model describes stepwise growth of a new phase at the interface with defect sites facilitating lithium ion migration [21]. In the mosaic model, domains of different composition make up the interphase, allowing lithium ions to conduct along grain boundaries. In the Coulombic model, positive lithium ions are bound to negatively charged carbon-containing ions, with the ionic bonding leading to enhanced stability of the layer. Even more models exist, yet all fall short of completely describing the formation of the SEI due to its complex nature.

While most study of SEI formation focuses on liquid electrolyte cells, the SEI can be an equally big challenge in solid-state batteries. Solid electrolytes still suffer from the same voltage issues

as liquid electrolytes, but other challenges exist, too. With all layers being solid, formation and dissolution of additional phases, especially if repeated every time the battery is cycled, can lead to cracking of some of the layers or loss of contact between the electrode and electrolyte. Furthermore, with relatively slow kinetics and potentially poor interfacial contact, lithium dendrite formation is a serious issue too [22]. When lithium ions preferentially deposit at certain locations at the interface, tree-like structures called dendrites can begin to form. If uncontrolled, these can quickly grow all the way from one electrode to the other, causing the battery to short-circuit. For batteries with liquid electrolytes, this can cause a fire. In any case, it will kill the functionality of the battery.

Even if lithium dendrites don't completely destroy the battery, SEI formation can lead to reduced performance and ultimately cell failure. As it forms, non-conductive material builds up at the interface, active material can become disconnected from the rest of the battery, and the contact area between layers is reduced. This is particularly a problem in cells with high-voltage cathodes or lithium metal anodes, where interfacial reactions can be severe if unchecked [23]. As such, mitigating the formation of SEI and controlling the SEI that does form is crucial for enhancing the lifetime of next-generation batteries.

II.II. SEI Mitigation

SEI formation is a complex process that, despite being the focus of considerable research in the past decades, is still not fully understood. With many factors affecting the process of SEI formation, including the electrolyte and electrode materials being used, applied current density, temperature, additives, surface morphology, it should be no surprise that there are also a

multitude of approaches for mitigation. These can be broadly divided into several main categories [24], with many other methods falling outside of these categories [25-27].

The first and perhaps most important way to mitigate SEI formation is through careful selection of the electrolyte material to begin with. In the case of organic liquid electrolytes, this has been a fairly fruitful approach as there are a wide variety of highly conductive liquids to choose from [28-30]. When it comes to solid electrolytes, this strategy is less effective due to the limited number of highly conductive solid electrolytes.

Another approach that has been highly effective for liquid electrolytes is the use of additives to mitigate SEI formation. These additives, usually mixed in low quantities to the electrolyte, suppress or control SEI formation in a variety of ways [31-33]. This approach does not translate well to solid electrolytes, however, as additives in a solid aren't free to migrate to the interfaces over time like they can in a liquid.

The approach with the most promise for solid-state batteries is the so-called artificial-SEI method (a-SEI) [34,35]. If a material with suitable properties – i.e. relatively high ionic conductivity, mechanical properties that allow good contact to be made, and a suitable voltage stability window – is placed between the electrolyte and electrode in a controlled manner, it should be able to stop the formation of an unwanted SEI altogether [36]. Though there may be a performance cost associated with the additional layer, it has the potential to greatly increase the lifetime of a cell.

II.III. LGPS Breakdown and SEI

Despite the promise of LGPS, over time a potentially severe flaw emerged. In 2016, Han et al. reported that despite previous claims, LGPS does in fact break down at both low and high voltages [37]. Rather than a potential window of -0.5 to 5 V vs Li, this new computational study found a potential window of 1.71 to 2.14 V vs. Li instead. Below 1.71 V Li_2S forms and above 2.14 V Ge_2S and S form, which can be very deleterious for cell performance. The authors cite poor interfacial contact, and subsequently poor reaction kinetics at the interface, as the reason why previous reports failed to observe any breakdown. Furthermore, the authors performed cyclic voltammetry on a Li/LGPS/LGPS-C/Pt cell in which significant amounts of a conductive carbon additive are mixed with the LGPS to greatly increase the contact and indeed, with this configuration, they found the breakdown outside of the predicted stability region.

II.IV. AlN as an a-SEI for LGPS

In this work, aluminum nitride is proposed as an a-SEI material for anodic protection of LGPS. AlN is a high bandgap semiconductor with high electrical resistivity and good air stability [38], which has been used extensively in the past for other applications such as optoelectronics and heat spreading [39,40]. Deposition of AlN via ALD has been documented in the past, with both highly pure and crystalline layers being grown with simple processes. Furthermore, computational and experimental work has been done showing the promise of AlN as a protection layer. AlN nanoflakes have been shown experimentally to suppress lithium dendrite formation [41]. Zhu et al. showed through DFT modeling that AlN may decompose to form Li_3N and Li_XAl when in contact with lithium. With Li_3N being a good lithium ion conductor, this interphase formation could enhance the cell performance compared to inert blocking layers. With this in

mind, the synthesis, characterization, and testing of AlN thin films is investigated in the context of LGPS-based solid state batteries.

Part III: Deposition and Characterization of AlN Films

III.I: Atomic Layer Deposition

Over the past decades, atomic layer deposition (ALD) has become the method of choice for depositing highly uniform and conformal thin films. First developed in the 1970s under the name atomic layer epitaxy, ALD is capable of creating films with sub-nanometer control over thickness and is able to evenly coat rough surfaces or surfaces with high aspect ratio features [42-44]. Though a wide variety of complex materials can be deposited via ALD, it excels primarily in the deposition of simple binary compounds, particularly oxides like Al_2O_3 and TiO_2 [45,46].

ALD is a variation of chemical vapor deposition in which the reactant gasses are sequentially pulsed onto the sample surface and then purged from the reaction chamber. During each pulse, the gas flowing over the sample reacts with ligands on the surface to form a new chemical species. The process is said to be self-limiting since once the gas has reacted with each ligand on the surface no further reactions occur. This causes growth to stop, and the surface is said to be saturated. The next precursor is then flowed over the sample, causing a new reaction to occur and for another layer of material to be deposited. Since the process is composed of discrete steps, controlling the number of ALD cycles that are performed allows for fine control over the final film thickness.

Due to the stepwise nature of the growth and the gaseous precursor delivery, ALD is exceptionally good at conformally coating surfaces with high roughness or high-aspect ratio features. Because of this, ALD is ideally suited for coating pores and other highly structured surfaces, and many results demonstrate even coating for features with aspect ratios greater than

100:1. In the case of LGPS pellets, high conformality is also extremely important. The rough surface of the pressed pellets contains many pore-like features which, if not coated in the protective material, may provide sites for degradation or dendrite growth to occur.

Most ALD processes need to be done at elevated temperatures in order to achieve optimal growth rates due to the activation energy of the reactions [47]. If the reactor temperature is too high, however, the reaction products may break down and form unwanted compounds. The ALD temperature window, therefore, is the region of temperatures in which saturated growth is achieved without any degradation of the product, and it is different for every process.

In some cases, reactive gas precursors can be ionized in what is referred to as plasma-enhanced ALD (PE-ALD). Since ionized gasses are much more reactive than when in the ground state, the temperature of the reaction can be lowered considerably. For example, SiO_2 growth via a PE-ALD process (AP-LTO + O_2 Plasma) achieved twice the growth rate as the comparable thermal ozone process, even with a 150 °C reduction in temperature [48]. PE-ALD does typically have the downside of lower conformality, as a plasma doesn't penetrate into pores as easily as a gas would.

III.II: ALD Aluminum Nitride

Despite being grown predominantly by molecular beam epitaxy in the past, ALD has become an attractive technique for AlN growth due to the relatively low temperatures - even for thermal processes. Since the early 2000s, AlN has been grown with ALD from a variety of precursors, with different processing conditions, and for a range of applications.

Though others have been reported [49], the most common precursors for ALD AlN are trimethylaluminum (TMA) and either nitrogen gas or ammonia, and both thermal and plasma-enhanced processes have been reported previously. Thermal processes are typically run above 400 °C to achieve the maximum growth rate, however this is not viable for our system. Previous testing on LGPS has found that deleterious side reactions begin to occur above 250 °C, which can lower the performance of the final pellet. To avoid this, plasma-enhanced ALD (PE-ALD) can be used to achieve suitably high growth rates at lower temperatures. Though still below the ALD window for the plasma process, previous reports suggest that plasma-enhanced deposition at 250 °C can achieve relatively high growth rates [50].

AlN is known to crystallize mainly into two structures, hexagonal (wurtzite) or cubic (zincblende) structures. Previous reports suggest that the ALD process produces polycrystalline wurtzite AlN, over a range of temperatures from 300 to 420 °C and both with and without plasma-enhancement [38,50,51].

ALD is also attractive for depositing AlN as it can create high purity films with good stoichiometry. Depending on the reactor design, precursors used, and temperature or plasma conditions, the Al:N ratio is typically 1:1.2 or better, with films typically being nitrogen-rich. While oxygen and carbon impurities are typically low (<5% total), some research suggests that PE-ALD may dramatically reduce oxygen and carbon impurities, which themselves disturb the Al:N ratio [52]. Other research suggests that NH_3 [53], and H_2 plasma to an even greater extent [51], contributes to removing carbon impurities by way of hydrogen interaction with the methyl groups in TMA.

III.III: Process Characterization

All ALD depositions were conducted in a Cambridge Nanotech Fiji F200 ALD reactor. The aluminum precursor selected was trimethylaluminum, which has the formula $(Al(CH_3)_3)_2$. Two sources were considered to introduce nitrogen into the film, nitrogen gas (N_2) and ammonia gas (NH_3), both of which were ionized to increase their reactivity. The processes were carried out at 250 °C, well below the standard process window for AlN, to ensure compatibility with LGPS substrates.

Initial characterization was carried out by running 300 cycles of both recipes on silicon test wafers. Film growth was monitored in situ using a J.A. Woolam M-2000 Spectroscopic Ellipsometer. These measurements are shown in Figure III.I. The pN_2 process exhibited linear growth over the course of the whole process, while the pNH_3 process exhibited a nucleation delay of roughly 50 cycles, followed by linear growth for the remainder of the process. In the linear regime, the growth rate is measured to be 0.64 Å/cycle for the pN_2 process and 0.78 Å/cycle for the pNH_3 process. With a rate of roughly 44 seconds per cycle in both cases, the overall growth rate is found to be 5.24 nm/hour and 6.53 nm/hour for the pN_2 and pNH_3 processes, respectively.

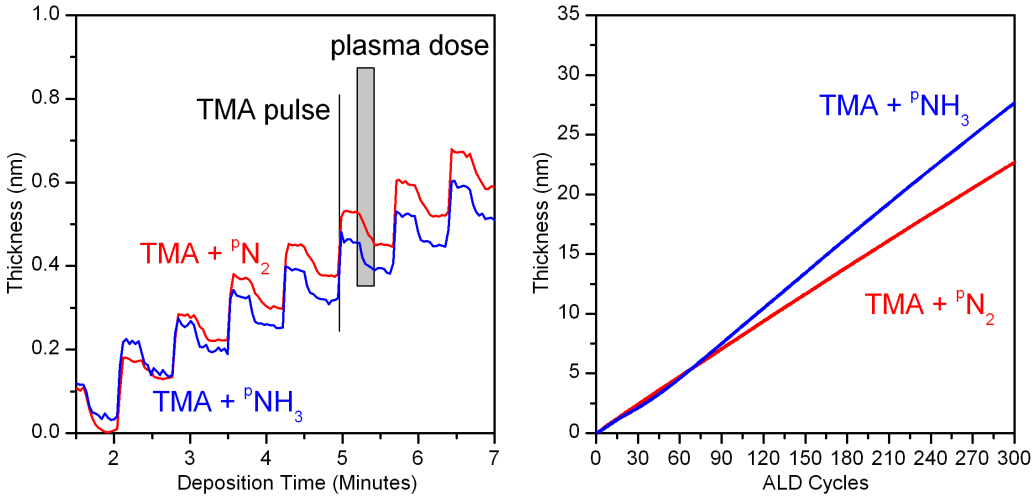

***Figure III.I**: Growth of AlN films via TMA and pN_s (red) and pNH_3 (blue) ALD obtained from in situ ellipsometry measurements. (Left) Inset of early cycles, highlighting the sub-monolayer growth behavior during each precursor pulse. (Right) Total growth over the whole process, showing the initial nucleation period followed by linear growth.*

Subsequently, SEM micrographs were used to verify film thickness. As shown in Figure III.II, a nominally 150 nm film of AlN can be seen to exhibit good thickness and uniformity over a several-micron distance.

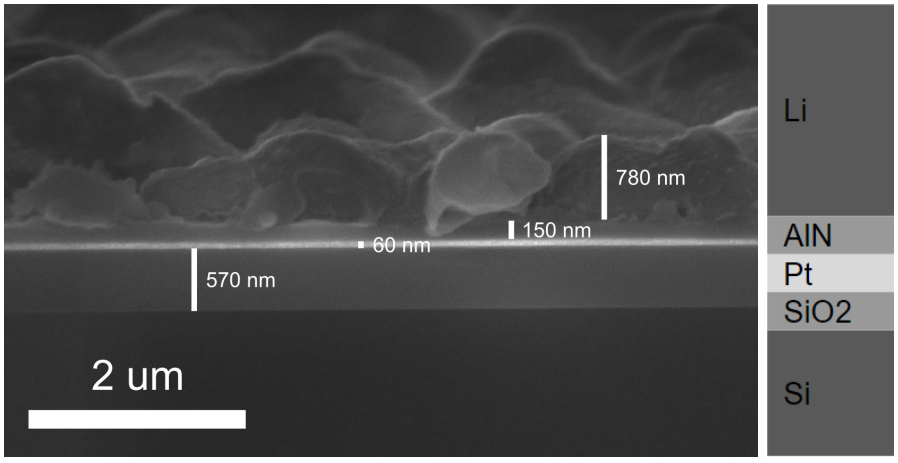

***Figure III.II**: (Left) An SEM micrograph of an AlN film in an Si/SiO_2/Pt/AlN/Li stack, with approximate layer thicknesses labeled.*

III.IV: Compositional Analysis

X-ray photoelectron spectroscopy (XPS) was performed to measure the composition of the deposited films and determine which precursor combination resulted in the highest quality film. XPS is a highly surface sensitive characterization technique that is capable of revealing chemical composition and bonding states for atoms in the top ~10 nm of a sample. This makes it ideal for analyzing the composition of thin films, however it also makes the measurements prone to interference from atmospheric contaminants, such as water and carbon, that rapidly adhere to the surface. To reduce contamination samples must be handled carefully and quickly, preferably staying in vacuum or glove box at all times. In addition to careful handling, surface contamination is mitigated by etching away the top few nanometers of material *in vacuo* with an argon plasma.

XPS measurements were taken with a Kratos Ultra DLD XPS using Al Kα (1486.6 eV) x-rays. The samples were kept under ultra-high vacuum ($<10^{-8}$ torr) for all measurements to avoid contamination. After the first measurement, samples were sputtered with argon plasma for a total of 4 minutes to remove surface contaminants.

The collected spectra were analyzed in CasaXPS using a Shirley background, a summed Gaussian-Lorentzian line shape, and relative sensitivity factors calibrated to our instrument specifications. Spectra were calibrated to C 1s (C-C) at 48.4 eV, except when no C-C peak was discernible, in which case the spectrum was calibrated to Al 2p (Al-N) at 73.5 eV [54]. Spin-orbit splitting subpeaks are merged for clarity in the Al 2p spectra. The collected spectra are shown in Figure III.III, and atomic percentages for each element are shown in Table III.I.

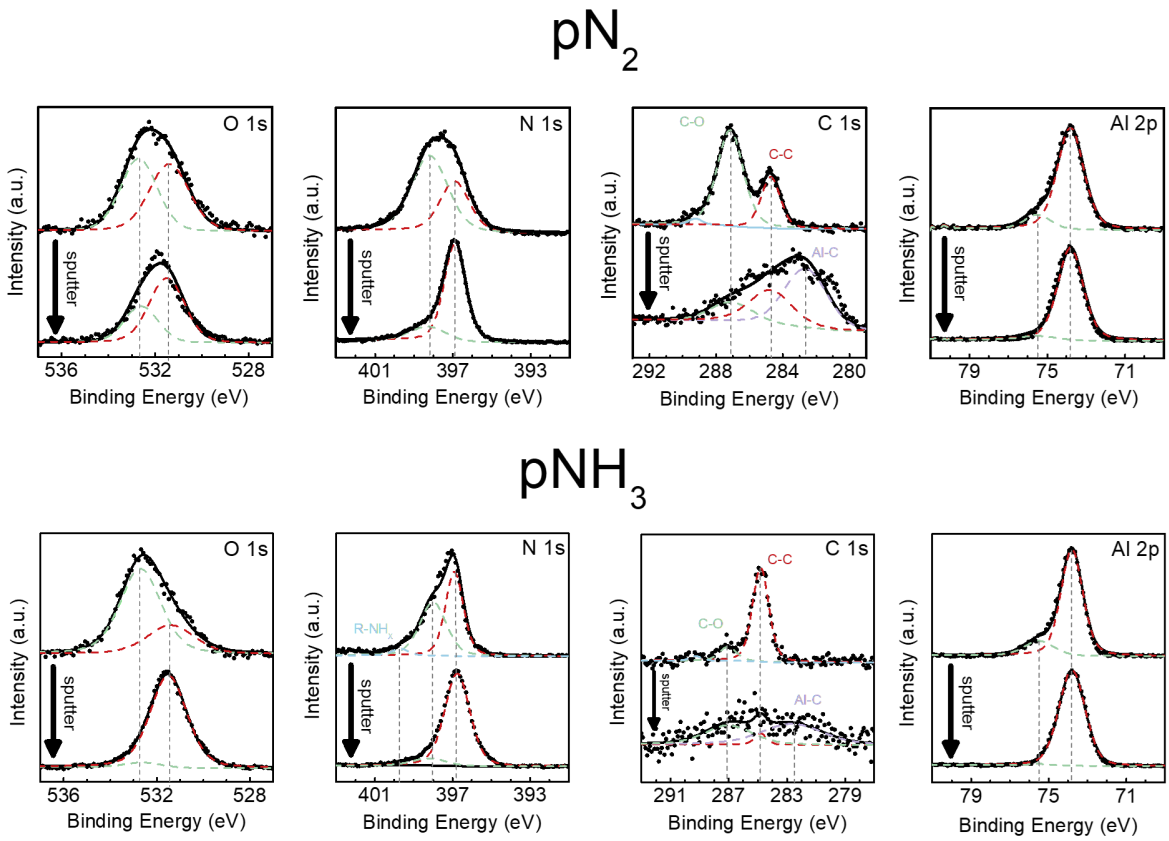

Figure III.III: *XPS of the AlN ALD process with pN_2 (top) versus pNH_3 (bottom) before (top inset) and after (bottom inset) four minutes of Ar^+ sputtering to remove surface impurities.*

	Al 2p (at%)	N 1s (at%)	O 1s (at%)	C 1s: (at%)
pN_2 (pre-etch):	35.2	36.3	9.8	18.9
pN_2 (post-etch):	46.4	30.8	11.8	11.1
pNH_3 (pre-etch):	48.4	30.6	8.9	12.2
pNH_3 (post-etch):	51.4	31.6	13.7	3.3

Table III.I*: Atomic percentages of each element found in the ALD-AlN films.*

In both pN_2 and pNH_3 samples, a decrease in carbon content and an increase in oxygen content is observed after sputtering. At the same time, the ratio of aluminum to other elements within the film becomes roughly 1:1 (1.01:1 and 1.06:1 for pN_2 and pNH_3, respectively) when surface impurities are removed. The lower carbon content in the pNH_3 sample, caused by the enhanced removal of methyl groups by hydrogen contained in the ammonia, supports previous findings. Due to the reduced carbon content, pNH_3 was used as the nitrogen source in further compositional analysis.

Previous reports on ALD-deposited AlN show good crystallinity when films are deposited at elevated temperatures (>350 C). To determine if the films grown at 250 °C also have crystallinity, Raman spectroscopy and XRD were performed, the results of which can be seen in Figure III.IV.

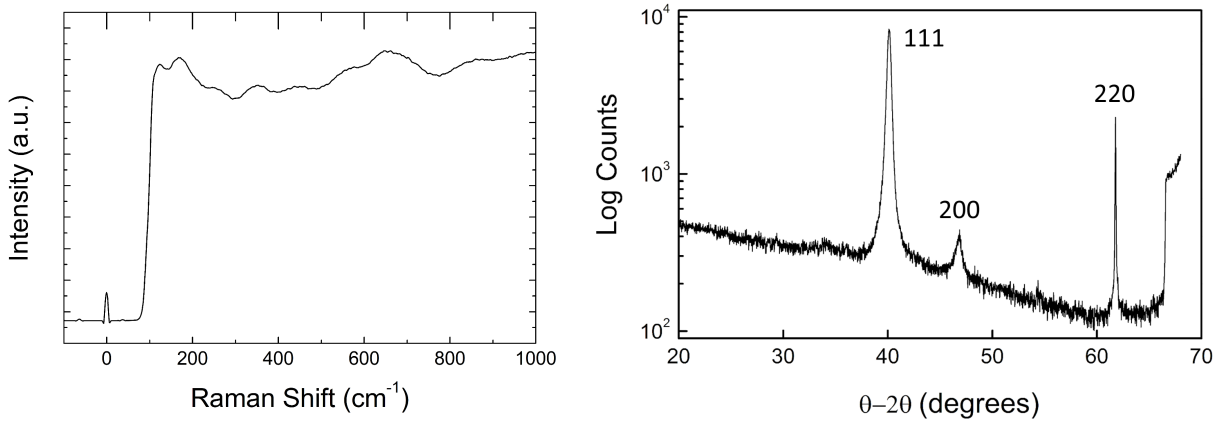

***Figure III.IV**: (Left) Raman spectrum and (right) x-ray diffraction pattern of pNH_3 AlN film.*

Raman spectra were collected using a Horiba LabRAM HR Evolution with a 532 nm laser source. Several broad and low intensity peaks can be identified in the spectrum. In the literature,

highly crystalline AlN films exhibit a strong peak at 650 cm^{-1} associated with the E_2^2 vibrational mode, as demonstrated by Oliveira et al. [55]. While a peak at 650 cm^{-1} can be identified in the collected spectrum, its low intensity and broadness indicates minimal - if any - crystalline domains are present in the film.

XRD measurements were collected using a Bruker D8 Advance diffractometer. The spectrum shows peaks at 40, 46 and 62 degrees, consistent with the (111), (200), and (220) reflections in Pt, the sample substrate. This is another indication that no crystalline AlN is present, which would result in clear peaks between 33 and 37 degrees.

III.V: Oxygen Contamination in PE-ALD AlN

In both samples, high oxygen content is observed both on the sample surface and in the bulk. Moreover, the relative oxygen content increases after sputtering, suggesting that the oxygen comes from the film itself and not from reaction with atmospheric gasses. Since there is no oxygen present in TMA or either plasma, the oxygen must come from some external source. A common source of oxygen impurities in PE-ALD is etching of the quartz tube in which the plasma is generated [56]. As the ions are generated and accelerated, some inevitably strike the walls of the tube and cause oxygen atoms present in the quartz (Al_2O_3) to be sputtered from the surface and ionized. These oxygen ions can then be accelerated down towards the sample and implanted in the film.

To verify this as the source of the oxygen impurity, an AlN film was first grown as normal with alternating TMA and pNH_3 cycles. The sample then received a post-treatment consisting of additional plasma pulses for several hours. After the film was grown, it was transferred through a glovebox into vacuum for XPS analysis. As with the previous samples, XPS spectra were

collected, then the sample was cleaned with argon plasma for four minutes before another set of XPS spectra were collected. The original pNH_3 spectra and the new spectra are shown in Figure III.V, with the quantification shown in Table III.II.

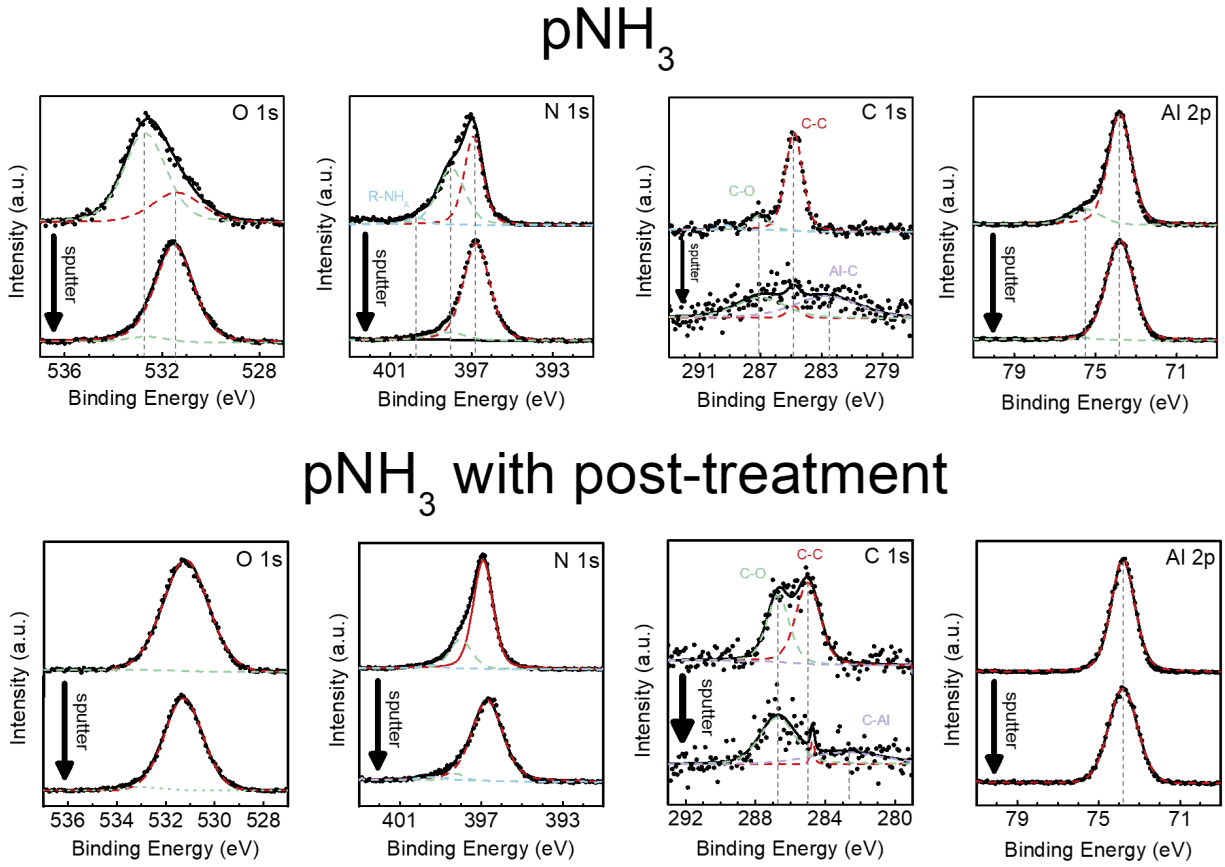

Figure III.V: *XPS of the original AlN ALD process with pNH_3 (top) versus the process with pNH_3 post-treatment (bottom), before (top inset) and after (bottom inset) Ar^+ etching.*

	Al 2p (at%)	N 1s (at%)	O 1s (at%)	C 1s: (at%)
No Post-treatment	51.6	31.6	13.6	3.2
Post-treatment	41.1	31.6	23.7	3.2

Table III.II*: Bulk composition of the pNH_3 films with and without post-treatment by ammonia plasma.*

The original pNH_3 sample has an Al:N:O:C ratio of 1 : 0.61 : 0.26 : 0.06, whereas the sample with post-treatment has a ratio of 1 : 0.77 : 0.58 : 0.08. Upon plasma exposure, there is a slight increase in bulk nitrogen content relative to aluminum, but a dramatic increase in the oxygen content. The carbon content is relatively unaffected. This verifies that the plasma step is responsible for much of the oxygen contamination found in the films.

III.VI: Growth on LGPS Substrates

AlN was also grown on LGPS pellets. LGPS powder purchased from MTI Corp. was pressed at 150 °C under 350 MPa of pressure. Full pellets were 600 μm thick with ~85% density. The full process is described by Wang et al. These pellets were then coated on both sides with nominally 75 nm of AlN using the pNH_3 process. After the deposition was completed one pellet was cleaved, and both cross sectional SEM and EDS mapping of the surface was obtained, as seen in Figure III.VI.

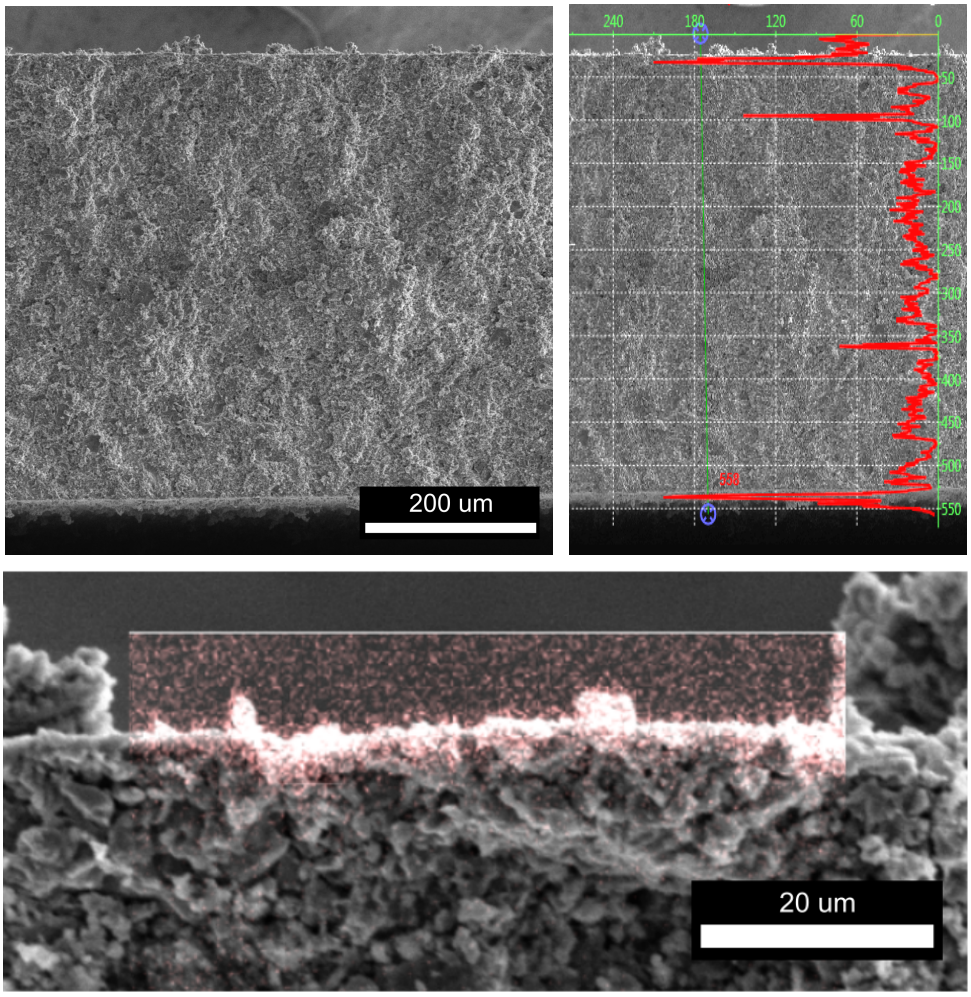

Figure III.VI: *(Top Left) Cross sectional SEM of LGPS pellet. (Top Right) EDS line scan of Al content across the width of the LGPS pellet, indicating elevated Al content on both surfaces. (Bottom) Cross sectional SEM of LGPS pellet with EDS map of Al overlaid in red, indicating AlN penetration of roughly 3 μm.*

The SEM cross section shows the porous bulk of the pellet as well as its uniform surface, a product of pressing at elevated temperature. The EDS line scan shows aluminum concentrated at the top and bottom surfaces, with other trace amounts likely due to the cleaving process. From the EDS map, it can be seen that the AlN has penetrated several microns into the LGPS pellet, which is in contrast to the 75 nm nominal film thickness. This discrepancy comes from several possible factors. For one, the porosity of the LGPS pellet may allow the gaseous precursors to

penetrate past the planar surface of the pellet into recesses and voids, producing deposition over a larger length scale. Depending on the porosity of the sample, this could result in almost no penetration or penetration of tens or hundreds of microns. Another explanation lies in the EDS measurement itself. The EDS technique relies on x-ray interactions with the electrons in the sample. Since x-rays may not be strongly absorbed by the sample, it can have a penetration depth of many microns. Then, if the sample is not exactly aligned to the detector, the misalignment of the x-rays can create the impression of depth where it does not exist.

Since the PE-ALD process used generally has worse conformality than thermal ALD process [57], it is unlikely that ammonia plasma significantly penetrates through pores and voids in the pellet. In this case, the thickness measured by EDS is likely due in large part to the tilting effects, and the film is more concentrated at the surface than it appears. In either case, these measurements place an upper limit on the penetration of AlN into LGPS, roughly 3 um, which is significantly smaller than the thickness of the pellet.

III.VII: Conclusions

Aluminum nitride grown from TMA and either N_2 or NH_3 plasmas at 250 °C is shown to exhibit a suitable growth rate given the reduced deposition temperature, with growth on both platinum and LGPS substrates observed. Compositionally, the use of ammonia has been shown to reduce carbon content, however the films still deviate significantly from literature in their oxygen content and crystallinity. Previous reports of ALD processes with similar, but not identical, recipes show oxygen content below 5 at%, whereas this process yields films with >10 at% oxygen. It has been shown that the plasma step in the ALD process contributed significant oxygen contamination, and without removal of that step it may not be possible to create purer

films. This process also produces amorphous AlN, as demonstrated through Raman spectroscopy and XRD measurements. This contrasts with literature reporting polycrystalline AlN at temperatures as low as 300 °C. It could be the case that the reduced temperature is the cause, but it may also be the case that the significant level of oxygen contamination hinders crystallization at this temperature. In order to create high-purity, crystalline AlN films by ALD, it may be necessary to increase the deposition temperature to 300 °C or greater, and not utilize plasma precursors. It may also be possible to replace the quartz tube-based plasma source with a stainless steel “hollow cathode” source, such as one described by Ozgit-Akgun et al. [58].

Part IV: Electrochemical Performance of Bare and Coated Electrolytes

IV.I: Background on Electrochemical Analysis

While commercial batteries can just be placed into a device and start delivering their power, when it comes to testing a battery or battery materials, there are many variables that can be controlled to learn different things about the system. Which electrodes are used, and how many, can greatly affect the thermodynamic behavior of the cell. Traditional batteries have one cathode and one anode, each a different material, but cells can be tested in two or three electrode setups, with different materials at each electrode or the same material used throughout.

When the same material is used for both electrodes in a two electrode setup, it is called a symmetric cell [59,60]. In this case, the materials are at equilibrium with each other when there is the same amount of lithium on both sides, and lithium transport can then only be driven by applying a potential to one electrode externally. The electrode with an externally applied voltage is called the working electrode, while the other is the counter electrode. In electrochemical testing, a potentiostat is used to control the voltage and current between these two electrodes, but what exactly is being controlled also affects the result of the test [61].

In galvanostatic operation, the amount of current being passed across the cell is controlled while the potential difference between the two electrodes is monitored and recorded. Current being passed means that lithium ions are transferred from one electrode to the other which will change the potential between them, reducing the potential at the electrode receiving lithium and raising the potential at the other electrode. There is always some potential associated with a given amount of lithium, as determined by thermodynamics, however in operation there are many other factors that can change the potential of the cell. In general, this results in an overpotential caused

by impedance in the cell. This could come from the limited conductivity of the electrolyte, activation energy associated with charge transfer reactions, or reduced concentration of charge carriers in certain regions [62]. Solid-electrolyte interphase formation contributes to this overpotential by forming a high-impedance layer between the electrode and electrolyte, so monitoring the overpotential in a galvanostatic cycling experiment can be helpful for understanding SEI formation.

Another method for probing the cell performance is electrochemical impedance spectroscopy, wherein an oscillating AC bias is applied to the cell, and the current response is measured. The amplitude and phase offset of this current response can then be used to determine the complex impedance of the cell over a range of frequencies. This can be used to understand what components of the cell are contributing to the impedance, since different reactions occur at different frequencies. Different mechanisms include electronic conduction in the electrodes, ionic conduction in the electrolyte, and charge transfer resistance at the boundary between the two, among others [63].

IV.II: Sample Preparation

All of the cells tested are in the two-electrode, symmetric cell configuration. Lithium metal, cut from a rod, is used for both electrodes, and LGPS is used as the electrolyte. Both bare and coated electrolytes are used in this test, however the assembly is identical in both cases. Stainless steel disks are used to both hold the cells in place and serve as current collectors for both electrodes. The Li/LGPS/Li stack is then sandwiched between two stainless steel disks, and placed into the split cell. Pressure is applied via a screw mechanism to maintain good contact between all layers, and clips are placed on the stainless steel current collectors to connect to a

potentiostat. The cells are assembled in a glovebox to avoid exposure of the lithium metal and LGPS to atmospheric contaminants, but once sealed the cells are brought into the atmosphere to be tested on a bench top.

IV.III: Bare LGPS Cycling

First, a bare-LGPS cell was cycled galvanostatically at a current density of 0.1 mA/cm^2. The discharge and charge half-cycles were each one hour long, for a total charge/discharge capacity of 0.1 mAh/cm^2. The cell was programmed to undergo 100 cycles, unless the overpotential reached a critical limit of +/-5 V, at which point cycling was discontinued. The cell overpotential is plotted versus time in Figure IV.I.

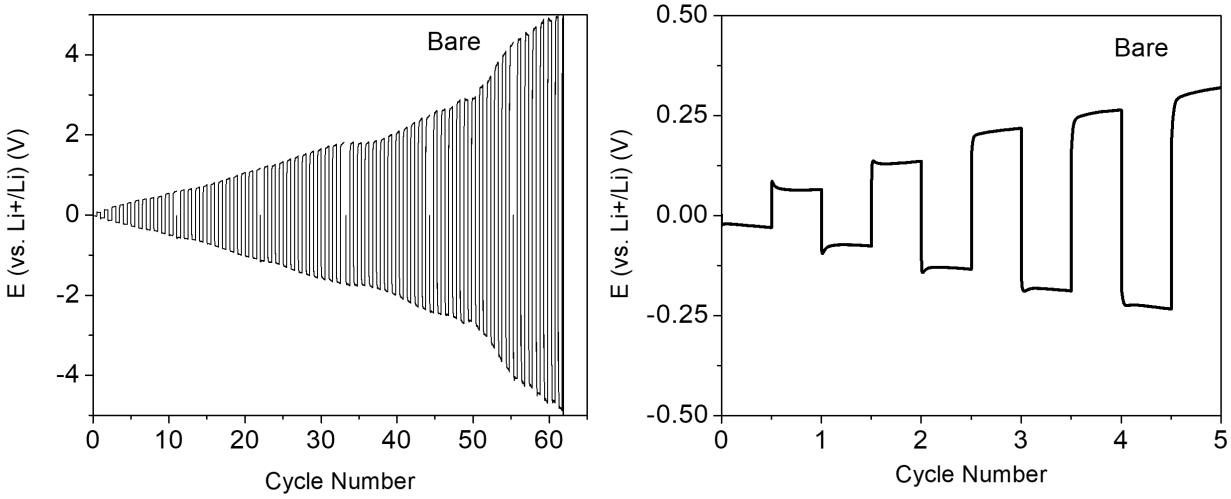

Figure IV.I: *(Left) Cell overpotential for the bare LGPS cell plotted for the duration of cycling. (Right) Inset of the cell overpotential for the first 5 cycles.*

From this figure, it can be seen that the cell with bare LGPS starts with minimal overpotential which rises consistently over the first 35 cycles, after which the cell rapidly degrades before failing at 62 cycles. This is characteristic of a first phase of slow SEI growth, followed by

uncontrolled rapid degradation once the SEI reaches a critical thickness. Once the overpotential increases too much and the SEI becomes too thick, the increased overpotential leads to enhanced breakdown at the interface, leading to rapid degradation and cell failure.

In addition to GV cycling, at the beginning of cycling and after every tenth cycle EIS was performed on the cell. The spectra were collected between 1 MHz to 10 mHz, with a 10 mV amplitude about the open circuit potential. The results of the EIS can be seen in Figure IV.II, showing the rapid increase in impedance before the cell ultimately fails.

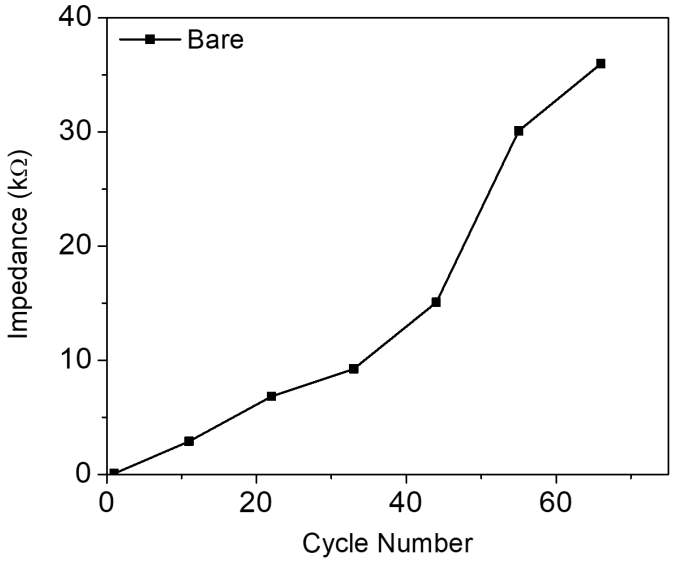

Figure IV.II: *Cell impedance measured by EIS initially and after every 10 cycles of the bare LGPS cell.*

IV.IV: Comparing pN_2- and pNH_3-AlN Protection Layers

Next, two cells are closed with a 20 nm coating of either pN_2-grown or pNH_3-grown AlN on the LGPS pellet. The cycling parameters remain the same as the first cell, and the comparison can be seen in Figure IV.III.

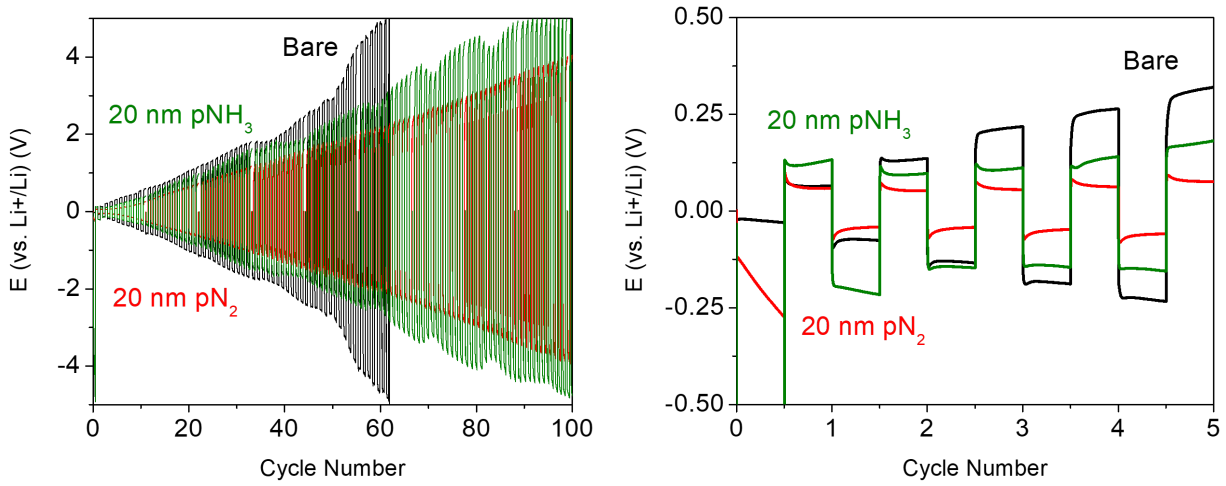

Figure IV.III: *(Left) Cell overpotential for the bare LGPS cell and both pN_2 and pNH_3 AlN-coated LGPS cells, plotted for the duration of cycling. (Right) Inset of the cell overpotential for the first 5 cycles.*

From this comparison, we can see that both the pN_2 and pNH_3 AlN-coated LGPS cells perform significantly better than the bare LGPS cell. The overpotential remains lower for the bulk of the cycling, and both cells were able to reach 100 cycles without failure caused by the overpotential increasing above the limit. Beyond just reducing the overpotential, there is also a difference in performance between the two protection layers. While the cell with pN_2-AlN cell shows a low initial overpotential and a steady increase over cycling, the pNH_3-AlN cell shows a high initial overpotential of nearly -5 V, which quickly returns to a normal value after only a couple of cycles. This increase in overpotential in this cell for the remaining cycles is much more erratic and nearly reaches the threshold at the end of cycling, suggesting it may not protect the interface as well as the pN_2-AlN does.

Analyzing the impedance from EIS, shown in Figure IV.IV, confirms the trend observed in the GV testing. Both coated cells start with a higher initial impedance, with the pNH_3-AlN cell

showing the highest at 4.2 kΩ. Over time, the bare cell's impedance increases the fastest, the pN_2-AlN cell increases slowly and steadily, and the pNH_3-AlN cell increases slightly faster and with less regular behavior.

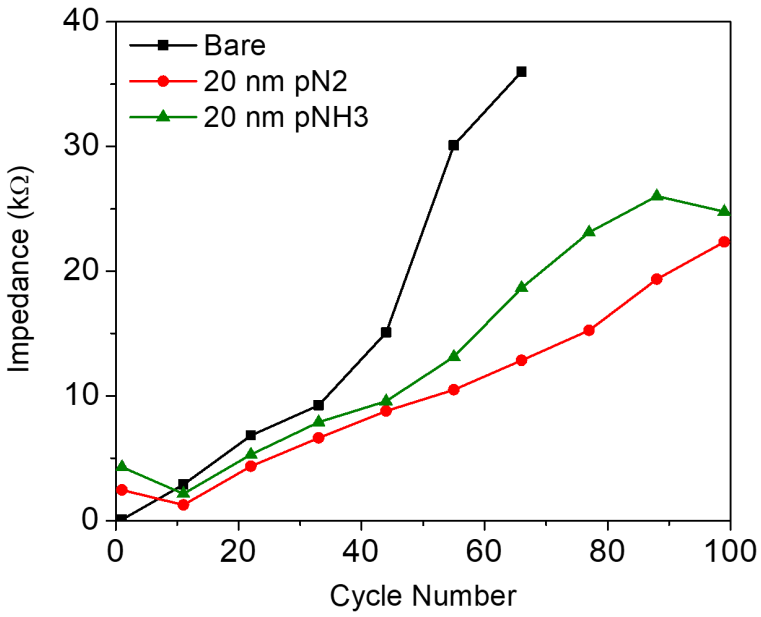

Figure IV.IV: *Cell impedance measured by EIS initially and after every 10 cycles of the bare LGPS cell and 20 nm AlN-coated cells.*

IV.V: The Effect of Coating Thickness on Cycling Performance

Finally, another cell is closed with a 75 nm coating of pNH_3-AlN. The cycling parameters remain the same as the first cell, but no EIS measurements were taken. The comparison can be seen in Figure IV.V.

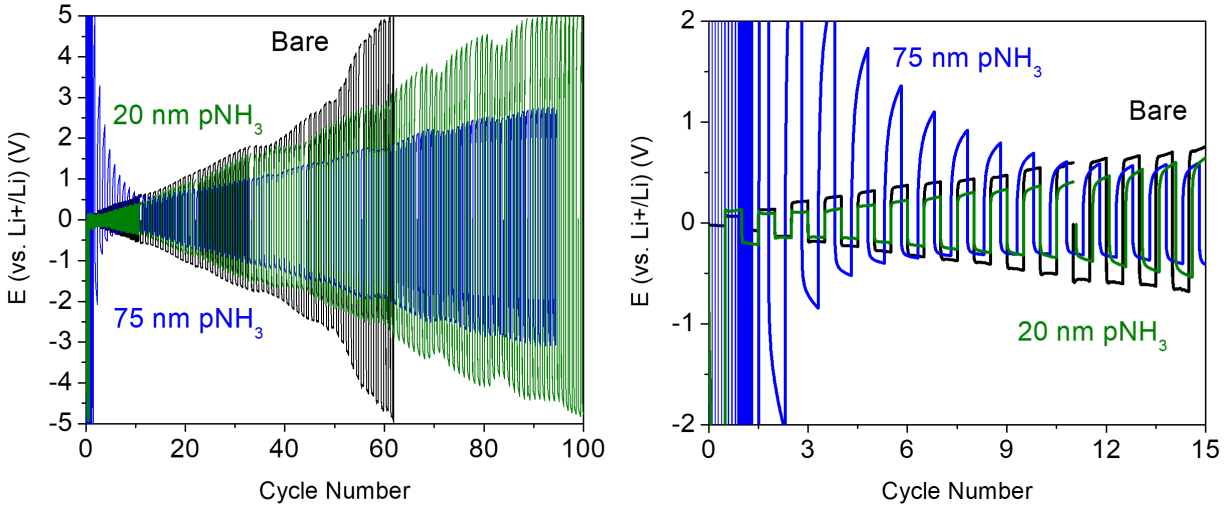

Figure IV.V: *(Left) Cell overpotential for the bare LGPS cell and both 20 nm and 75 nm pNH_3 AlN-coated LGPS cells, plotted for the duration of cycling. (Right) Inset of the cell overpotential for the first 15 cycles.*

The final cell with a 75 nm pNH_3-AlN coating shows the most interesting behavior. Initially, the overpotential is very high, reaching 5 V. After roughly ten cycles, however, the overpotential decreases back to the level of the other cells, and for the remainder of cycling it actually has the lowest overpotential. Although it was stopped early for unrelated reasons, extrapolating from the collected data suggests that this cell may be able to survive up to 200 cycles before reaching the overpotential limit, more than tripling the performance of the bare cell.

IV.VI: Conclusions

From this electrochemical testing, it can clearly be seen that AlN coatings of varying sorts can be effective as a protection layer by reducing the overpotential and increasing the cycle lifetime of cells. That being said, the different types and thicknesses of AlN tested all exhibit different behavior, which raises more questions about the function of the AlN protection layer.

Despite containing the highest level of carbon impurities, the AlN grown with pN_2 shows the most consistent behavior during cycling, with an extremely linear increase in overpotential. It is also much more effective at reducing the overpotential of the cell when compared to a cell of similar thickness grown with pNH_3. This finding raises questions about what in the protection layer is actually responsible for the improved performance. The initial expectation that Li_3N formation will confer the best properties, while any impurities that contribute to Li_2O or Li_2CO_3 formation should hinder the performance, may not have been correct. The fact that the film with more impurities had better performance puts this into question. Could it be the case that these unwanted oxide and carbonate products actually benefit cell performance? Or is it the case that the reactions occurring in the interphase are more complicated than they may seem, and that the pN_2 film actually forms more Li_3N despite having impurities? Further experiments are needed to address these questions.

Comparing the performance of the different thicknesses also raises interesting questions. In the sample with a 20 nm pNH_3-AlN coating, a high overpotential is observed for the first half-cycle, but the overpotential quickly returns to the expected range. In the simple with a 75 nm coating, the initially high overpotential remains for roughly ten cycles before decaying back to the expected range, suggesting that whatever process is contributing to the high initial overpotential depends on the thickness of the coating. One possible explanation for this behavior is that there is a break-in period at the start of cycling in which the AlN becomes lithiated to form Li_3N or any other products. If this process depends on the diffusion of lithium, it would be expected that the length of the break-in period is dependent on the thickness. While more work is needed to determine whether this is the mechanism at play, post-mortem compositional analysis, or

analysis on cells disassembled during the break-in period, would be best for understanding this phenomenon.

Part V: Lithiation of AlN via Evaporation of Lithium Metal

V.I: Sample Preparation

In order to investigate the lithiation of AlN, several devices were made. One centimeter-square chips were diced from a Pt-coated thermal oxide wafer to use as substrates for the devices. 150 nm of AlN was then deposited via the pNH_3 ALD process with a resulting Al:N:O ratio of 1: 0.58: 0.27, consistent with previous depositions. A shadow mask was used to prevent deposition around the edges of the chips, as shown in Figure V.I, which allows for electrical contact with the bottom platinum current collector in future devices.

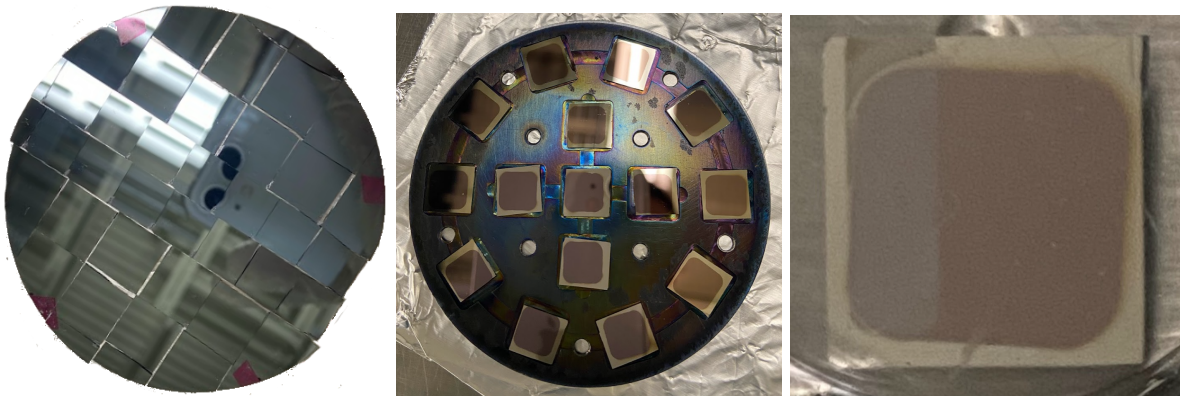

Figure V.I: *(Left) As-diced Pt-coated silicon wafer. (Center) Pt-coated silicon chips with AlN coating. (Right) Pt-coated silicon chip with AlN and Li.*

Lithium metal was deposited onto the chips via thermal evaporation in a custom-built system. The evaporator has a base pressure of $<5x10^{-9}$ torr and is connected to the glovebox, which is critical for limiting the reaction of lithium metal with atmospheric gasses to form lithium carbonate, oxide, or hydroxide.

The evaporation is conducted at 400 °C with an approximate growth rate of 12 nm/minute as measured by quartz crystal microbalance. As such, approximately 720 nm of Li metal was deposited over the course of one hour. SEM images of the samples in Figure V.II indicate the lithium is continuous, with a rough surface morphology showing bubbles characteristic of lithium metal deposited in this way [64,65]. Despite the uneven surface, the thickness of both the lithium and AlN layers match expectations, verifying the capabilities of both deposition methods.

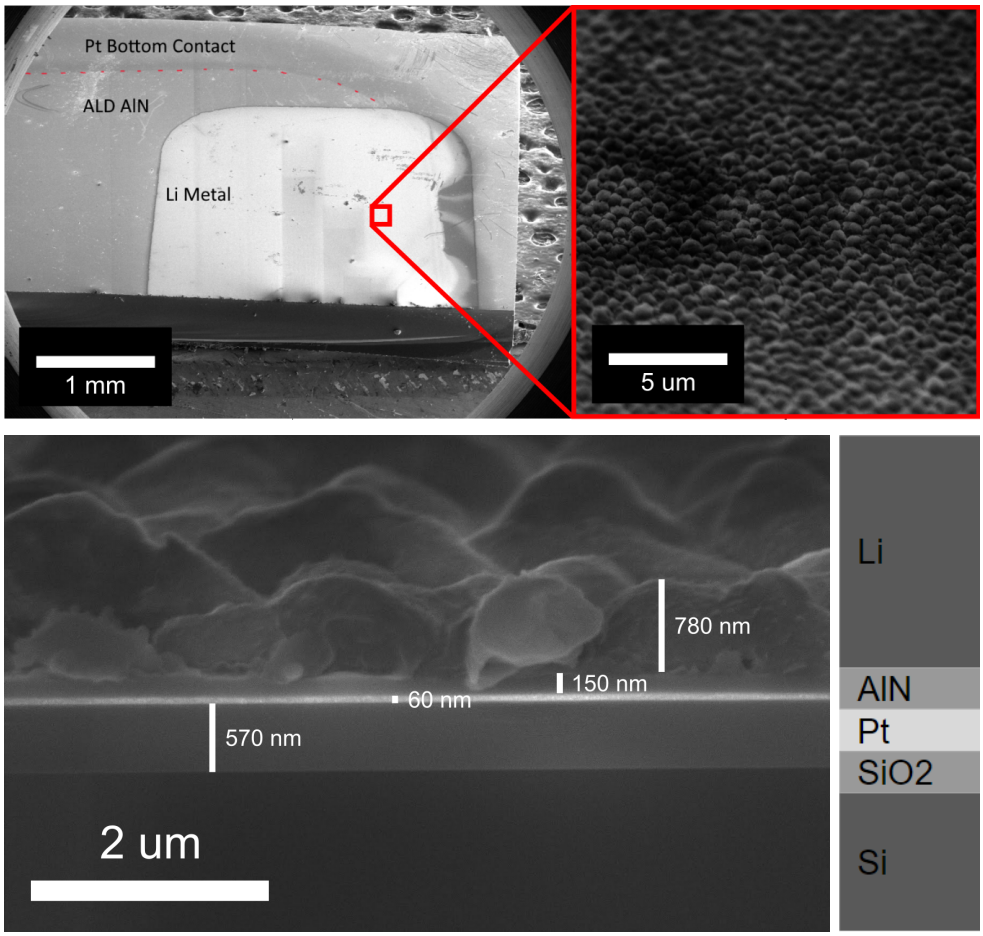

Figure V.II: *(Top left) Field view SEM image of Li metal pad on AlN on Pt. (Top right) High resolution SEM of Li metal surface, showing coverage and morphology. (Bottom left) Cross-sectional SEM image of Li metal on AlN on Pt with (Bottom right) a schematic of the layer structure.*

V.II: XPS Analysis of Lateral Li/AlN Reaction

When the lithium metal is evaporated onto AlN, chemical reactions at the interface and diffusion through the material occur. As the lithium diffuses into and reacts with the AlN, this device geometry should create a uniform reaction front across the length of the chip. By measuring this composition with XPS, an understanding of the interaction between lithium and AlN can be formed.

Once the lithium is evaporated onto the chip, it is transferred into vacuum and then the surface is cleaned with argon plasma. To measure the evolution of the concentration gradient, an XPS line scan is performed, starting on the lithium pad and extending into the AlN region. Seven points are selected on the AlN, with a spacing of 0.25 mm, and scans are taken every twelve hours over the course of one week. A selection of the results can be seen in Figure V.III.

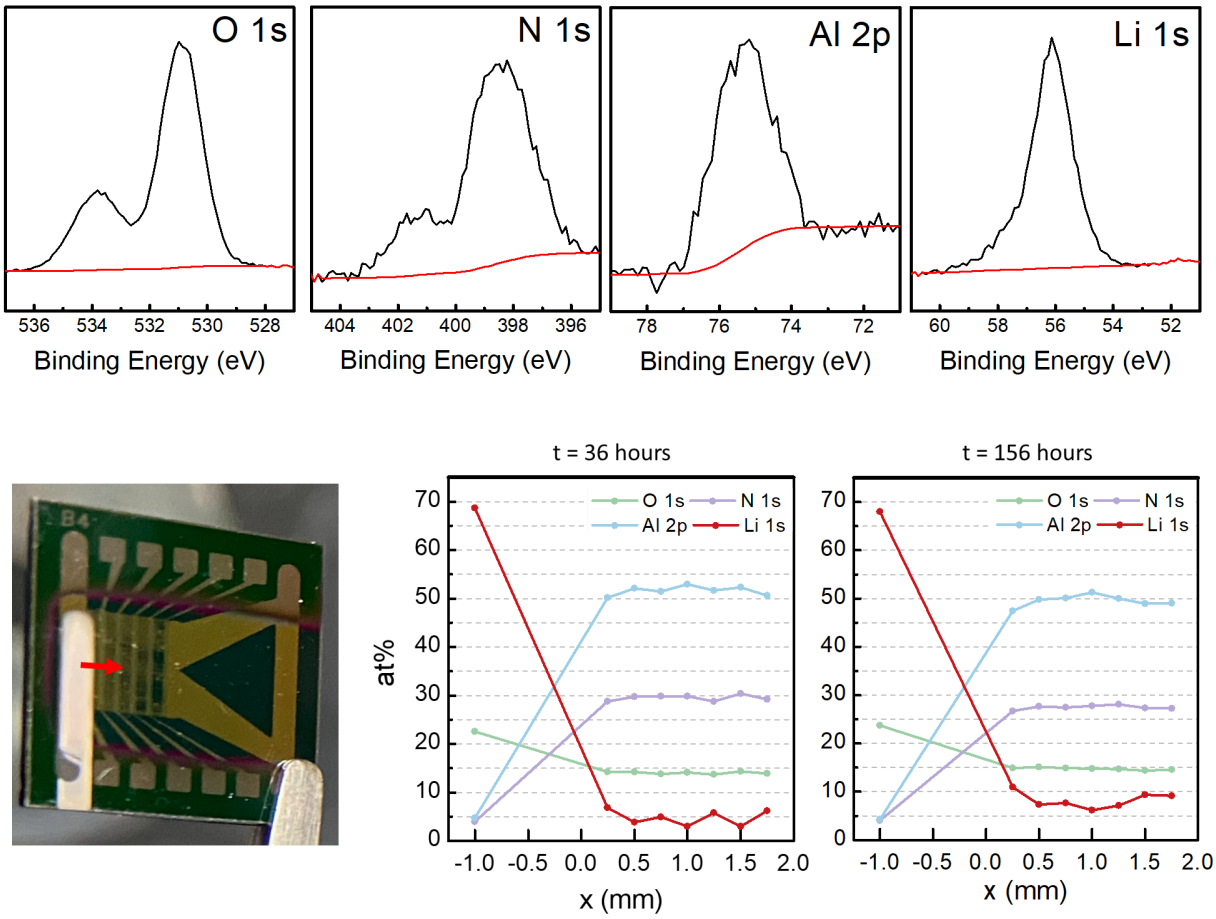

Figure V.III. *(Top) High resolution spectra. (Bottom left) A photo of a similar device with the line scan position highlighted by a red arrow, and the lateral composition profiles at first and last time steps.*

Each spectrum is found to contain Al, N, Li, O, and C, however in all spectra the carbon content is a roughly constant background value between 2 and 4 at%, so it is not considered in this analysis. The spot on the lithium pad shows 65 to 70 at% Li, 20 to 25 at% O, and trace amounts of the remainder. This is consistent with previous results from the tool, indicating moderately high quality lithium has been deposited. The other spots have a roughly uniform composition with roughly 50 at% Al, 25 to 30 at% N, 15 at% O, and the remaining 5 to 10 at% being lithium.

This Al:N:O ratio comes out to roughly 1 : 0.56 : 0.28, which is consistent with the calibration runs described previously.

The lithiation behavior is further examined by isolating the lithium trace from each line scan, as seen in Figure V.IV. Despite a clear trend of increasing lithium content with time, the high level of noise limits interpretability. To increase clarity, the spots from each line scan are averaged, and the average lithium content is plotted versus time. From this, it can be clearly seen that the atomic percentage of lithium in the film increases from 5.5 to 8.3. The standard error of the mean is also plotted, showing that while the trend is small, it is greater than the noise.

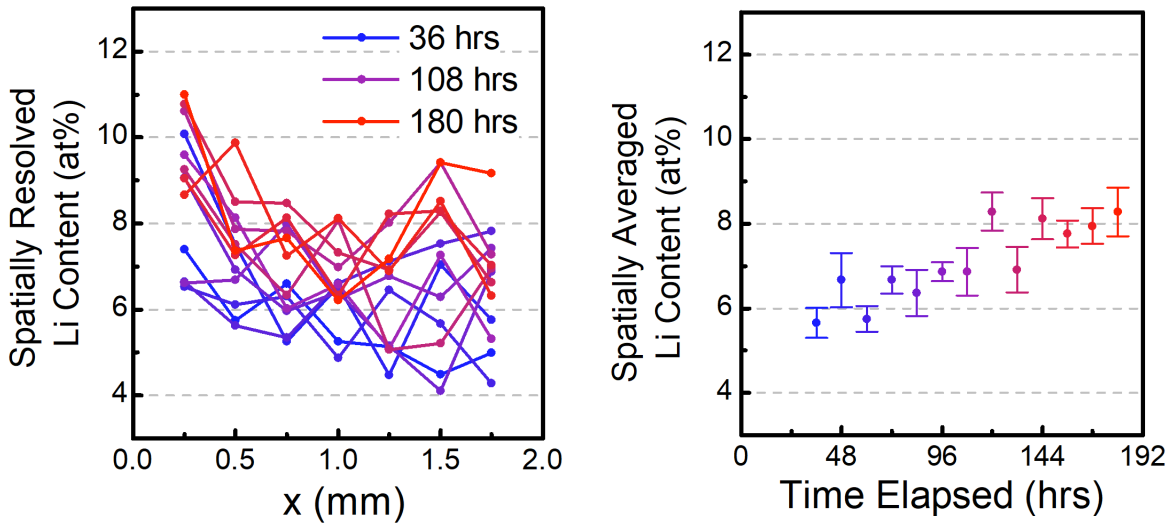

Figure V.IV. *(Left) Atomic percentage of lithium over the length of the line scan, for times ranging from 36 to 180 hours at 12 hour increments, as measured by XPS. (Right) The average lithium content for each line scan ranging from 0.25 to 1.75 mm, versus the time elapsed since deposition.*

V.III: Simulating Lithiation Behavior with COMSOL Finite Element Analysis

To better understand the behavior of the Li/AlN lateral reaction system, a finite element model was constructed using COMSOL Multiphysics. COMSOL is a continuum mechanical modeling software which allows for physics-based equations to be solved over custom geometries and boundary conditions.

For this model, the Transport of Dilute Species interface is used which contains equations for Fickian diffusion. A one-dimensional geometry is constructed to mimic the shape of the line scan, with a mesh consisting of evenly spaced elements along the line. A positive flux of solute atoms, representing lithium atoms, is applied to the boundary at x = 0 mm, and the solute is subsequently allowed to diffuse across the line. Both the flux across the interface and the diffusion coefficient are controlled by Arrenhius-type equations of the form

$$F = F_0 exp(-E_a/RT)$$

where E_a is the activation energy of the process and F_0 is a pre-exponential term.

In addition to these parameters of the model, the temperature is programmed to mimic that of the real samples. As such, it starts at an elevated temperature of 400 ^oC where it is held for one hour, the same length of time as the evaporation. After that point, the temperature decreases gradually to room temperature where it is held for the remainder. This behavior can be altered, however, to reproduce different evaporation conditions or even post-deposition heat treatments.

In addition to producing a simulated concentration gradient over time, the model also calculates the average lithium concentration from x = 0.25 to 1.75 mm, which was the other metric used in the previous section. With these metrics defined, the model was run and the Arrhenius equation

parameters were adjusted until the results closely matched the experimental results, as shown in Figure V.V.

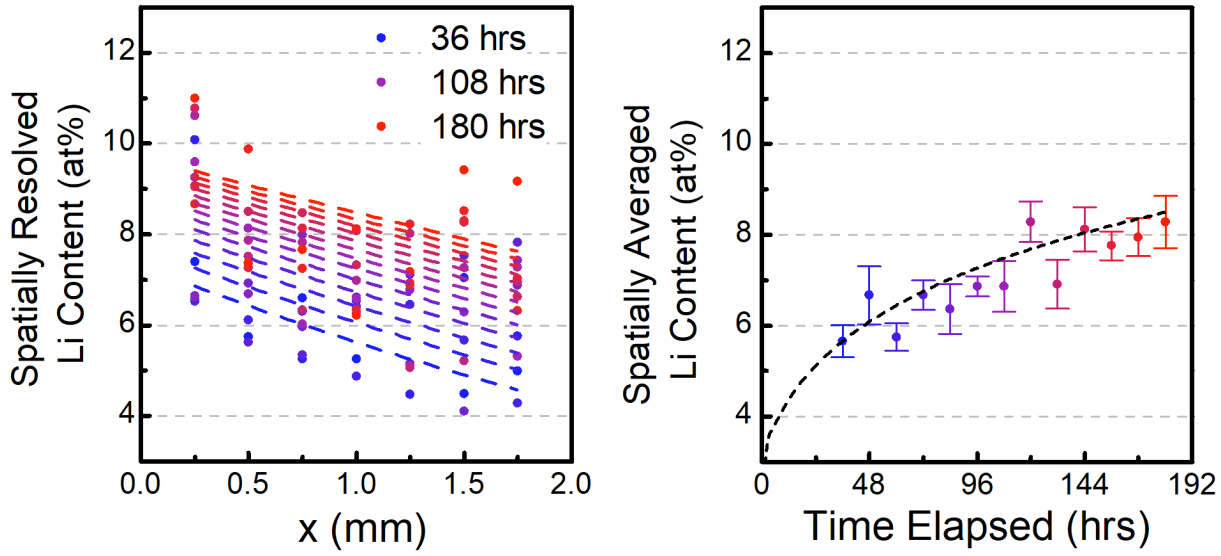

Figure V.V. *(Left) Experimental (points) and computed (dashed lines) lithium content for each line scan. (Right) Average lithium content over time for the experimental (points) and computed (dashed line) data.*

The parameters resulting in the above fit are $D_0 = 2x10^{-7}$ m^2/s, $E_a = 0.22$ eV, $k_0 = 3x10^{-6}$ m/s and $E_k = 0.15$ eV. This model output shows that the model is able to closely replicate the experimentally observed results with only basic physics being included. However, it may be the case that the model is overfitted to the data, and cannot be extrapolated to other scenarios.

In order to further test the model, two more simulations are run. First, simulations are run with a post-deposition heat treatment. 48 hours after evaporation, the sample is heated to a target temperature and held for another 48 hours before cooling back to room temperature. The target temperatures range from 20 °C (no treatment) to 100 °C. The results can be seen in Figure V.VI

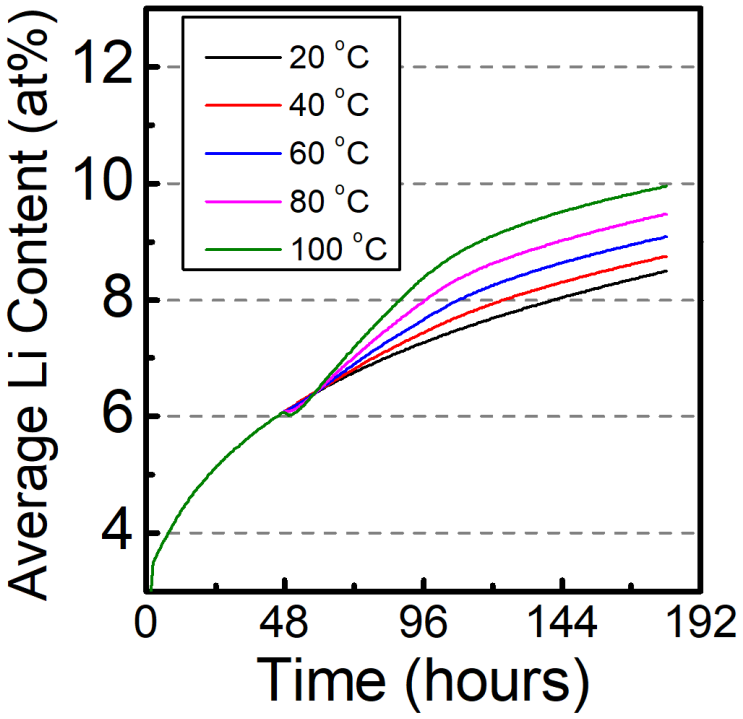

Figure V.VI. *Predicted average lithium content for a sample with a 48 hour post-annealing step done 48 hours after deposition, with the annealing temperature ranging from 20 °C to 100 °C.*

From this it can be seen that the average lithium content over the region increases significantly (roughly 1.2x) after a 48 hour post-treatment at 100 °C. Replicating this experimentally would provide a straightforward way to validate that the model is generalizable to different scenarios. If these results can't be replicated experimentally, it may suggest that there is more occurring within the samples - chemical reactions, interaction with impurity species, etc. - that significantly affects the observable behavior.

Next, simulations are run with varying evaporation temperatures and times. First, initial calibration data obtained via quartz crystal microbalance is used to determine the relationship between deposition temperature and growth rate for the lithium evaporator. From Figure V.VII, it

can be seen that this follows an exponential relationship, where the growth rate as a function of deposition temperature can be modeled as:

$$R(T) = 2.72 \times 10^{-6} exp(0.033\,T)$$

with an excellent fit to the data (R^2=0.9999). With this relationship, the temperature ramp in the model is then adjusted so that the length of evaporation varies with temperature to produce a constant thickness. The model is then run over a range of temperatures to simulate evaporations of 1 um of lithium metal, and the composition profile is analyzed for each case.

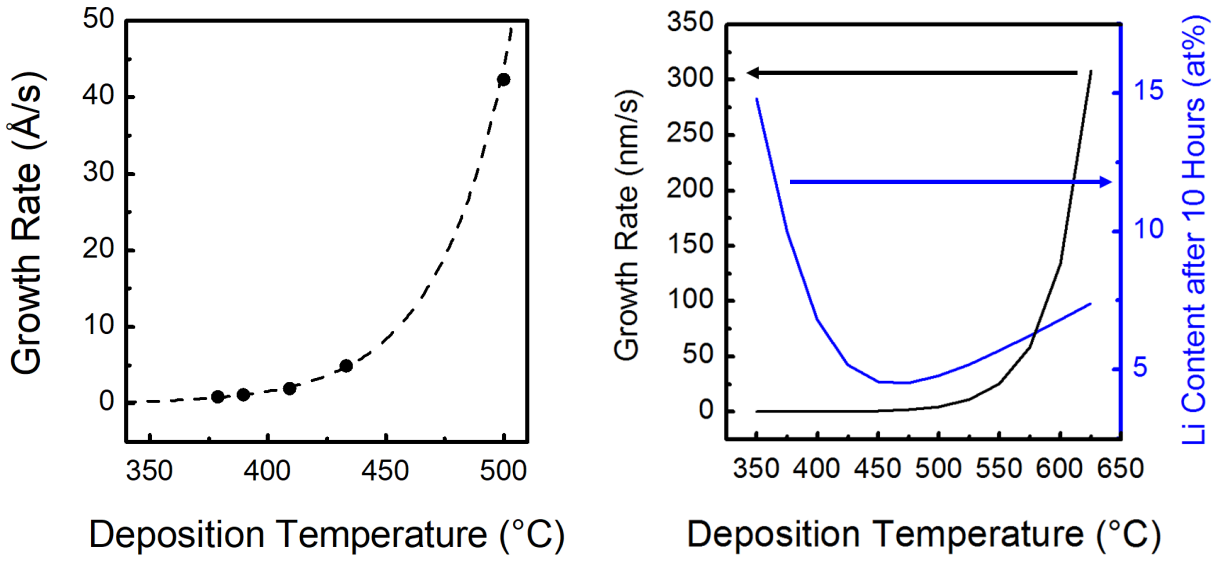

Figure IV.VII. *(Left) Measured growth rate (points) and exponential fit (dashed line) from QCM data. (Right) Growth rate as a function of temperature from fit (black) and predicted lithium content 10 hours after deposition as a function of deposition temperature (blue).*

From the blue curve on Figure V.VII, it can be seen that there is actually a minimum in the average lithium content after deposition that occurs around 450 to 475 °C. This aligns closely with the conventional knowledge that evaporating lithium around 500 °C results in the least heat

transfer to the sample due to the fast rate of deposition. This also means that control over the evaporation temperature can be a useful tool for tuning the lithium content in the film for future experiments.

V.IV: Li/AlN Conductivity Measurements using the Lateral Test Platform

In addition to chips with a blanket Pt bottom contact, devices were made on a lateral test platform with interdigitated Pt electrodes. These structures consist of two Pt electrodes at the top and bottom of the chip for applying lateral bias, and five pairs of interdigitated electrodes on either side of the chip for performing conductivity measurements. More details of the geometry, as well as optical and SEM images of the device, can be seen in Figure V.VIII. On this device, the pairs of electrodes are spaced 1 mm apart. The fingers extend 995 um, and are 5 um wide, creating a 5 um gap between them on all sides. Although the features created are sharp, missing fingers can clearly be seen in both optical and SEM images of the device due to poor adhesion of the Pt layer.

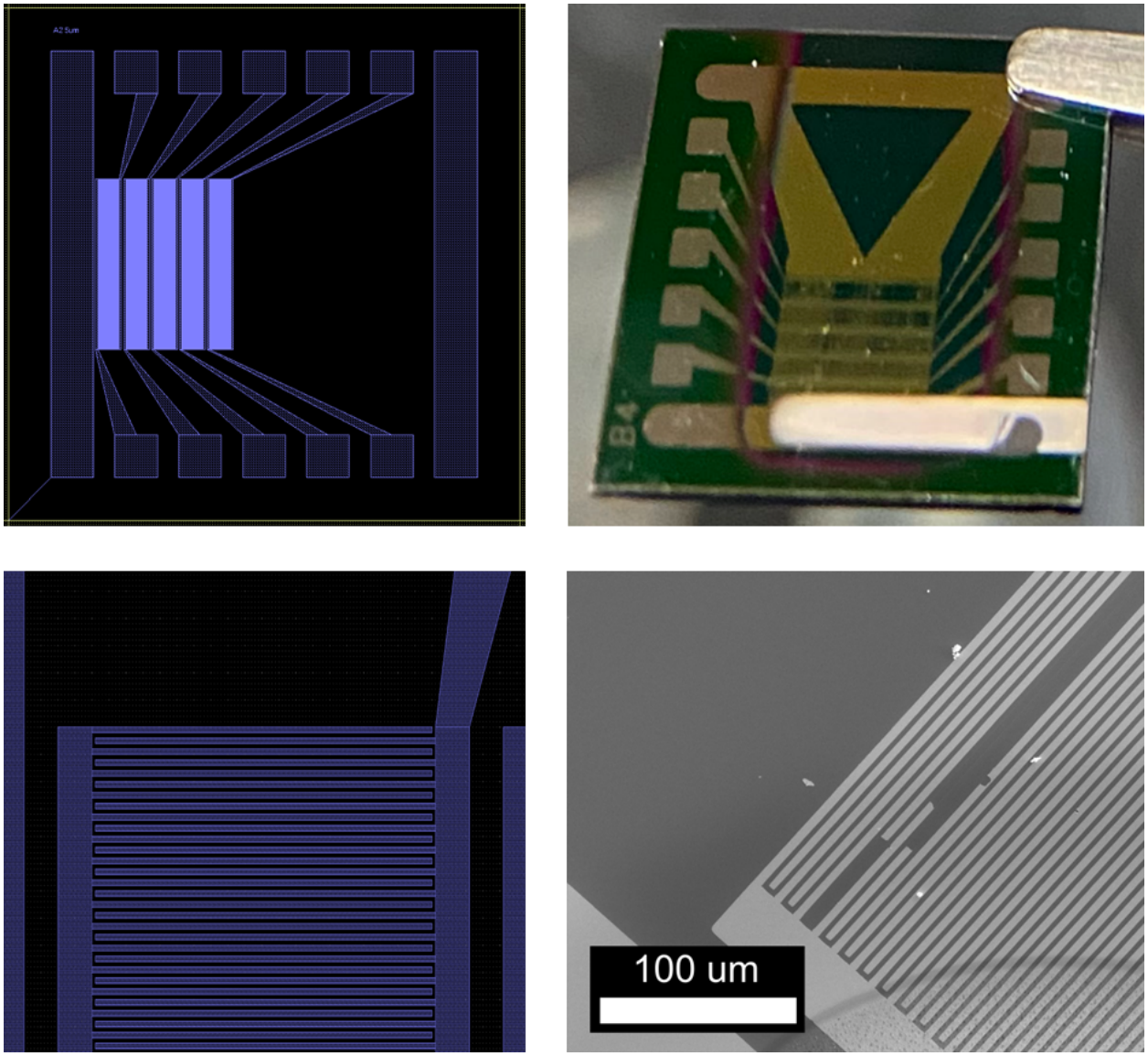

Figure V.VIII. *(Left) CAD rendering of device design. (Top right) a photo of a device after fabrication is complete, and (Bottom right) an SEM image of the interdigitated electrodes, highlighting missing fingers.*

To analyze the electrochemical properties of the Li/AlN, EIS was performed on each pair of pads over the course of three days. EIS was performed in potentiostatic mode at the open circuit voltage, with an AC bias with +/- 100 mV amplitude applied over the frequency range 100 kHz

to 1 kHz. For all measurements taken, the spectra have a similar shape, which can be seen in the bottom left of Figure V.IX. At low frequencies, there is a positive real impedance on the order of several hundred ohms, and the phase angle is zero. As the frequency increases, both the impedance and the phase angle increase. This increase in phase angle means that the current response of the circuit is offset from the applied voltage, which indicates there is some capacitance in the system. That being said, the phase angle stays far below 90^{o} - the phase angle expected from a capacitor - even at the highest frequencies achievable by the potentiostat used.

Typically, devices whose equivalent circuit is a resistor and capacitor in parallel exhibit a semicircular spectrum with the high frequency side being at the lowest impedance. This is the behavior typically seen in batteries and many capacitors. This is opposite to the behavior we see, suggesting that the Li/AlN is behaving quite differently from a conventional dielectric.

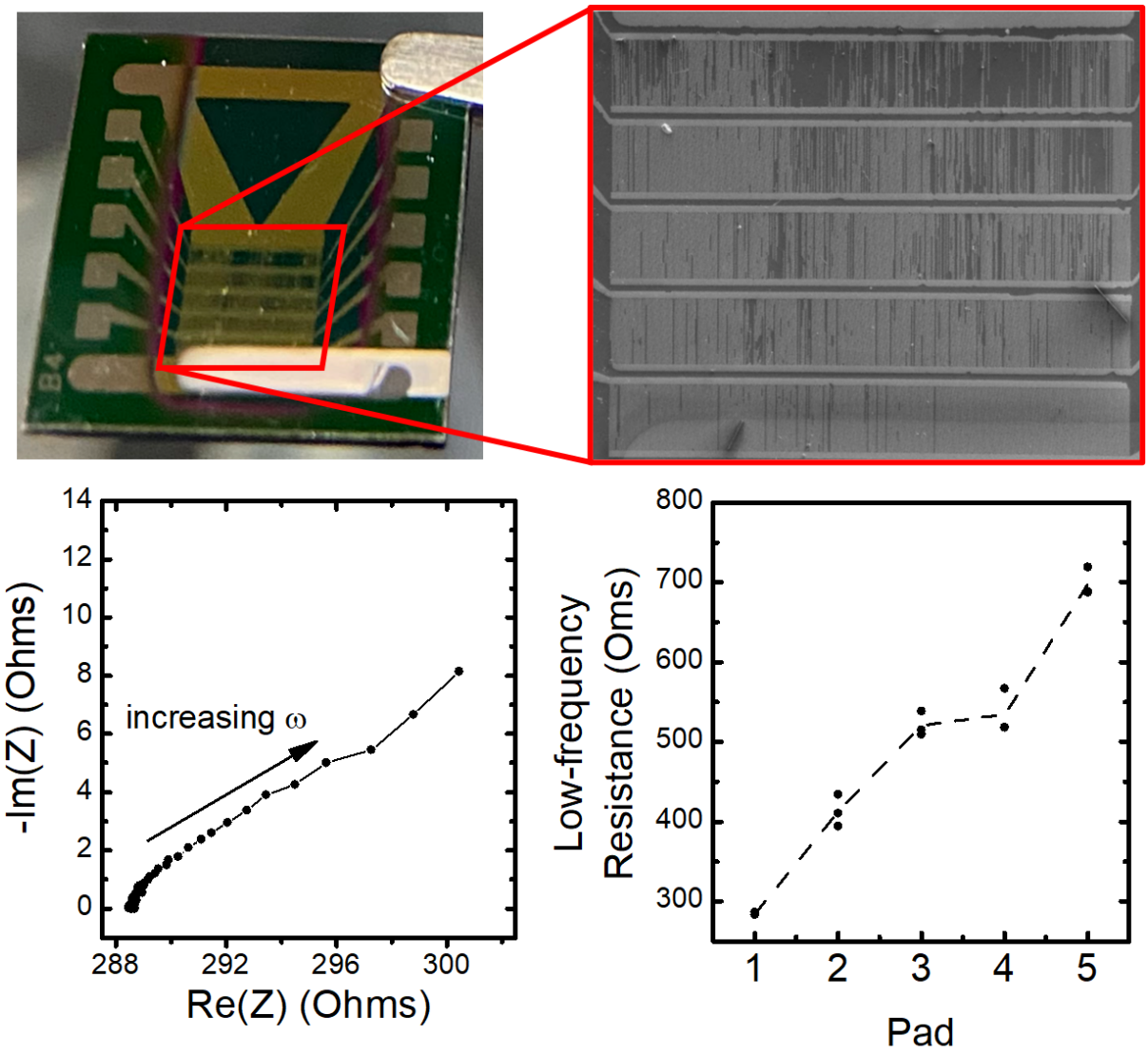

Figure V.IX: *(Top left) Photo of interdigitated device with (Top right) an SEM image of the highlighted region showing missing pads. (Bottom left) An example electrochemical impedance spectrum from one pair of pads and (Bottom right) the low-frequency impedance extracted from each spectrum.*

Aside from the unusual shape of the spectra, the low-frequency resistance of each pair of pads is quite consistent both measurement to measurement and day to day, as shown in the bottom right of Figure IV.VIII. The change in resistance from pad to pad, increasing with distance from the

lithium source, can be explained by the missing Pt fingers. The SEM image shows that the electrode pair closest to the lithium pad has the largest number of intact fingers, with the number decreasing with each subsequent pad.

V.V: Conclusions

Based on this work, it is clear that AlN does not rapidly react with evaporated lithium metal under ambient conditions, or even at elevated temperatures. While the lithiation process does seem to be thermally activated, even when lithium is evaporated onto AlN at 400 °C, the AlN is able to maintain its morphology and thickness. This is in contrast to some other potential protection layer materials, such as LiPON. When lithium metal is evaporated onto LiPON, there can be extensive damage to the protection layer including swelling and delamination. The fact that AlN exhibits good robustness makes it more attractive.

The slow rate of lithiation may not be as attractive, however. In order for the material to serve as a protection layer, it must be both stable against lithium metal and ionically conductive enough that it doesn't cripple the cell performance. If lithium diffuses through the material very slowly, it may be the case that the AlN protection layer will contribute too much impedance to the cell.

There are, however, still many unanswered questions regarding this. For one, the experiments performed here feature length scales of millimeters, as opposed to the nanometers or microns found in solid state batteries. It may be the case that lithiation happens fast enough through the depth of the film, but not over such large lateral distances. Secondly, these experiments don't feature any electrochemically-driven lithiation. In a battery, there is an applied driving force pushing lithium through the material, which is absent in these experiments. It may be the case that this driving force is enough to speed up the lithium migration. It may also be the case that,

upon applying a potential to the layers, new species are formed which can't be accounted for in these experiments.

Therefore, while these experiments lay out the groundwork for studying lithiation in a material like AlN, they by no means paint the full picture. If anything, they highlight the fact that more work should be done to understand the mechanisms behind lithiation and lithium motion in AlN.

Part VI. Summary of Work and Future Outlook of AlN-Protected LGPS Electrolytes

VI.I. AlN ALD Process

This work has demonstrated that previously developed recipes for atomic layer deposition of AlN are somewhat effective when the temperature is reduced to 250 °C, but fail to create high purity, polycrystalline films. Using ammonia plasma reduces the bulk carbon content of the films as previous works claim, however the oxygen contamination remains significant. It has been demonstrated that the plasma step is a significant source of oxygen contamination, however the plasma step is also necessary to improve the growth rate without surpassing the upper limit of the LGPS' temperature stability window. It is unclear how the presence of oxygen or carbon contaminants affects the performance of AlN as a protection layer, however it is clear that it makes understanding the mechanisms at play in lithiation much more complex.

Moving forward, examination of how the process parameters affect oxygen content in the final films is needed. This may involve testing the recipe with non-plasma NH_3 to determine how the oxygen content is reduced and how the growth rate is affected, pushing the temperature higher towards the optimal range reported in previous literature, or possibly even experimenting with other precursors, such as $AlCl_3$ or H_2.

Additionally, developing an Li_3N ALD process is not only essential for coating LGPS in highly conductive protection layers, but would open the door for a whole new set of experiments with pre-lithiated AlN. Digital doping of multiple ALD precursors, in which cycles of two processes

are alternated in some fixed ratio, could enable precise and uniform titration of lithium through the AlN film, yielding high quality samples for electrochemical tests.

VI.II. Integrating AlN into Batteries

This work has shown that AlN is able to protect the anode-electrolyte interface in a solid state battery and enhance performance. Cells with AlN-coated electrolyte pellets are able to cycle for more cycles than their unprotected counterparts, and with a lower overpotential. At the same time, the effect of thickness and film composition remain somewhat unclear, with thick pNH_3-AlN films and relatively impure pN_2-AlN films showing lower overpotential in the long term.

Furthermore, large initial impedance followed by a break in period of several cycles has been observed in the thicker films. It is believed that this corresponds to lithiation of the AlN during the initial cycling, however it is not clear exactly what reactions are occurring, nor how this break-in period scales with film thickness or affects the overall impedance as the cell continues to cycle. Testing more cell configurations, with different thicknesses of AlN and different cycling conditions, may help to elucidate this. Additionally, studying model systems such as the lateral platform, can simplify the experiments so complications associated with cycling a full cell can be eliminated.

VI.III. Lithiation of AlN

This work has demonstrated that AlN is stable against evaporated lithium, showing slow diffusion on the length scale of millimeters only after a week's time. More experiments on the temperature-dependence of diffusion are necessary to cement the understanding, however a finite

element model has been constructed which can guide future experiments in this direction. Different evaporation temperatures and times should be tested, as well as post-evaporation thermal processing. Additionally, placing lithium in contact with AlN without elevated temperature, and then monitoring diffusion over time, should be done as a control.

Furthermore, little has been done to investigate the effect of electrochemically-driven diffusion. In a battery system, this may end up being the primary driver of diffusion, rather than elevated temperatures, so studying this phenomenon in a model system such as the lateral test structure is important.

The difficulty in analyzing lithiation behavior also further highlights the importance of creating high purity AlN films. With significant contamination from oxygen and carbon, it becomes exceedingly difficult to deconvolute the different reactions, and subsequent different chemical species present in an XPS spectrum. Starting with high purity AlN would allow the careful study of what specific Li-Al-N species form at different states of lithiation, especially as the ability to control the diffusion is enhanced.

References

[1] Brown, G., Chan, B., Clune, R. & Cutler, Z. Upgrade the grid: Speed is of the essence in the energy transition. McKinsey & Company (2022). Available at: https://www.mckinsey.com/business-functions/operations/our-insights/global-infrastructure-initiative/voices/upgrade-the-grid-speed-is-of-the-essence-in-the-energy-transition.

[2] Greim, P., Solomon, A. A. & Breyer, C. Assessment of lithium criticality in the global energy transition and addressing policy gaps in transportation. Nature Communications 11, (2020).

[3] Friedman, D. The role of the Chemical Sciences in finding alternatives to critical resources: A workshop summary. (National Academies Press, 2012).

[4] Olivetti, E. A., Ceder, G., Gaustad, G. G. & Fu, X. Lithium-ion battery supply chain considerations: Analysis of potential bottlenecks in critical metals. Joule 1, 229–243 (2017).

[5] Battery Critical Materials Supply Chain Challenges and Opportunities, Department of Energy Office of Energy Efficiency & Renewable Energy (2022)

[6] Mongird, K. et al. 2020 Grid Energy Storage Technology Cost and Performance Assessment, Department of Energy (2020).

[7] Cole, W., Frazier, W. & Augustine, C. Cost Projections for Utility-Scale Battery Storage: 2021 Update. Available at: https://www.nrel.gov/docs/fy21osti/79236.pdf.

[8] Sun, P., Bisschop, R., Niu, H. & Huang, X. A review of battery fires in electric vehicles. Fire Technology 56, 1361–1410 (2020).

[9] Samuelson, K. A brief history of Samsung's failed Galaxy Note 7 smartphone. Time (2016). Available at: https://time.com/4526350/samsung-galaxy-note-7-recall-problems-overheating-fire/

[10] The history of electrochemistry: From Volta to to Edison. ECS (2016). Available at: https://www.electrochem.org/birth-of-electrochemistry.

[11] Whittingham, M. S. Intercalation chemistry and Energy Storage. Journal of Solid State Chemistry 29, 303–310 (1979).

[12] Reddy, M. V., Mauger, A., Julien, C. M., Paolella, A. & Zaghib, K. Brief history of early lithium-battery development. Materials 13, 1884 (2020).

[13] Kong, L., Li, C., Jiang, J. & Pecht, M. Li-ion battery fire hazards and Safety Strategies. Energies 11, 2191 (2018).

[14] Liang, C. C. & Bro, P. A high-voltage, solid-state battery system I . Design Considerations. Journal of The Electrochemical Society 116, 1322 (1969).

[15] Liang, C. C., Epstein, J. & Boyle, G. H. A High‐Voltage, Solid‐State Battery System: II . Fabrication of Thin‐Film Cells. Journal of The Electrochemical Society 116, 1452 (1969).

[16] Alpen, U. v., Rabenau, A. & Talat, G. H. Ionic conductivity in Li3N single crystals. Applied Physics Letters 30, (1977).

[17] Ren, Y. et al. Oxide Electrolytes for Lithium Batteries. Journal of the American Chemical Society 98, 3603–3623 (2015).

[18] Kanno, R. & Murayama, M. Lithium Ionic conductor thio-LISICON: The Li_2S-GeS_2-P_2S_5 system. Journal of The Electrochemical Society 148, (2001).

[19] Kamaya, N. et al. A lithium superionic conductor. Nature Materials 10, (2011).

[20] Cheng, X.-B. et al. A review of solid electrolyte Interphases on lithium metal anode. Advanced Science 3, 1500213 (2015).

[21] Peled, E. The electrochemical behavior of alkali and alkaline earth metals in nonaqueous battery systems—the solid electrolyte interphase model. Journal of The Electrochemical Society 126, 2047–2051 (1979).

[22] Lou, S. et al. Interface issues and challenges in all‐solid‐state batteries: Lithium, sodium, and beyond. Advanced Materials 33, 2000721 (2020).

[23] Bieker, G., Winter, M. & Bieker, P. Electrochemical in situ investigations of Sei and Dendrite Formation on the lithium metal anode. Physical Chemistry Chemical Physics 17, 8670–8679 (2015).

[24] Cheng, X.-B. et al. A review of solid electrolyte Interphases on lithium metal anode. Advanced Science 3, (2016).

[25] Ding, F. et al. Dendrite-free lithium deposition via self-healing electrostatic shield mechanism. Journal of the American Chemical Society 135, 4450–4456 (2013).

[26] Kim, J. S. & Yoon, W. Y. Improvement in lithium cycling efficiency by using lithium powder anode. Electrochimica Acta 50, 531–534 (2004).

[27] Cheng, X.-B., Peng, H.-J., Huang, J.-Q., Wei, F. & Zhang, Q. Dendrite-free nanostructured anode: Entrapment of lithium in a 3D fibrous matrix for ultra-stable lithium-sulfur batteries. Small (2014). doi:10.1002/smll.201401837

[28] Bommier, C. & Ji, X. Electrolytes, sei formation, and binders: A review of nonelectrode factors for sodium‐ion battery anodes. Small 14, 1703576 (2018).

[29] Yang, C. R., Wang, Y. Y. & Wan, C. C. Composition analysis of the passive film on the carbon electrode of a lithium-ion battery with an EC-based electrolyte. Journal of Power Sources 72, 66–70 (1998).

[30] Gofer, Y., Ben-Zion, M. & Aurbach, D. Solutions of $LiAsF_6$ in 1,3-dioxolane for secondary lithium batteries. Journal of Power Sources 39, 163–178 (1992).

[31] Ming, J. et al. New insight on the role of electrolyte additives in rechargeable lithium ion batteries. ACS Energy Letters 4, (2019).

[32] Möller, K.-C. et al. In situ characterization of the SEI formation on graphite in the presence of a vinylene group containing film-forming electrolyte additives. Journal of Power Sources 119-121, 561–566 (2003).

[33] Jankowski, P., Wieczorek, W. & Johansson, P. SEI-forming electrolyte additives for lithium-ion batteries: Development and benchmarking of computational approaches. Journal of Molecular Modeling 23, (2016).

[34] Kato, A., Hayashi, A. & Tatsumisago, M. Enhancing utilization of lithium metal electrodes in all-solid-state batteries by interface modification with Gold Thin Films. Journal of Power Sources 309, 27–32 (2016).

[35] Dudney, N. J. Addition of a thin-film inorganic solid electrolyte (lipon) as a protective film in lithium batteries with a liquid electrolyte. Journal of Power Sources 89, 176–179 (2000).

[36] Paul, P. P. et al. Interfaces in all solid state Li-metal batteries: A review on instabilities, Stabilization Strategies, and scalability. Energy Storage Materials 45, 969–1001 (2022).

[37] Ha, F., Zhu, Y., He, X., Mo, Y. & Wang, C. Electrochemical Stability of $Li_{10}GeP_2S_{12}$ and $Li_7La_3Zr_2O_{12}$ Solid Electrolytes. Advanced Energy Materials (2016).

[38] Banerjee, S., Aarnink, A. A., van de Kruijs, R., Kovalgin, A. Y. & Schmitz, J. Peald AlN: Controlling growth and film crystallinity. physica status solidi (c) 12, 1036–1042 (2015).

[39] Jmerik, V., Toropov, A., Davydov, V. & Ivanov, S. Monolayer‐thick GaN/AlN multilayer heterostructures for deep‐ultraviolet optoelectronics. physica status solidi (RRL) – Rapid Research Letters 15, 2100242 (2021).

[40] Tsurumi, N. et al. AlN Passivation over algan/gan hfets for surface heat spreading. IEEE Transactions on Electron Devices 57, 980–985 (2010).

[41] Gao, C. et al. Self‐suppression of lithium dendrite with aluminum nitride Nanoflake additive in 3D carbon paper for Lithium Metal Batteries. Energy Technology 8, 1901463 (2020).

[42] Zazpe, R. et al. Atomic layer deposition for coating of high aspect ratio TiO_2 nanotube layers. Langmuir 32, 10551–10558 (2016).

[43] Knez, M., Nielsch, K. & Niinistoe, L. Cheminform abstract: Synthesis and surface engineering of complex nanostructures by atomic layer deposition. ChemInform 39, (2008).

[44] Fang, W.-Z. et al. Atomic layer deposition in porous electrodes: A pore-scale modeling study. Chemical Engineering Journal 378, 122099 (2019).

[45] Groner, M. D., Fabreguette, F. H., Elam, J. W. & George, S. M. Low-Temperature Al_2O_3 Atomic Layer Deposition. Chemistry of Materials (2004).

[46] Aarik, J., Aidla, A., Uustare, T. & Sammelselg, V. Morphology and structure of TiO_2 thin films grown by atomic layer deposition. Journal of Crystal Growth 148, 268–275 (1995).

[47] Johnson, R. W., Hultqvist, A. & Bent, S. F. A brief review of atomic layer deposition: From fundamentals to applications. Materials Today 17, 236–246 (2014).

[48] Putkonen, M. et al. Thermal and plasma enhanced atomic layer deposition of SiO_2 using commercial silicon precursors. Thin Solid Films 558, 93–98 (2014).

[49] Lee, Y. J. & Kang, S.-W. Growth of aluminum nitride thin films prepared by plasma-enhanced atomic layer deposition. Thin Solid Films 446, 227–231 (2004).

[50] Liu, X., Ramanathan, S., Lee, E. & Seidel, T. E. Atomic layer deposition of aluminum nitride thin films from trimethyl aluminum (TMA) and ammonia. MRS Proceedings 811, (2004).

[51] Tian, L. et al. Aluminum nitride thin films deposited by hydrogen plasma enhanced and thermal atomic layer deposition. Surface and Coatings Technology 347, 181–190 (2018).

[52] Detavernier, C., Dendooven, J., Deduytsche, D. & Musschoot, J. Thermal versus plasma-enhanced ALD: Growth Kinetics and conformality. ECS Transactions 16, 239–246 (2008).

[53] Ozgit, C., Donmez, I., Alevli, M. & Biyikli, N. Self-limiting low-temperature growth of crystalline aln thin films by plasma-enhanced atomic layer deposition. Thin Solid Films 520, 2750–2755 (2012).

[54] Rosenberger, L., Baird, R., McCullen, E., Auner, G. & Shreve, G. XPS analysis of aluminum nitride films deposited by plasma source molecular beam epitaxy. Surface and Interface Analysis 40, 1254–1261 (2008).

[55] Oliveira, I. C., Otani, C., Maciel, H. S., Noda, L. K. & Temperini, M. L. A. Raman active E_2 modes in aluminum nitride films. Journal of Materials Science: Materials in Electronics 12, (2001).

[56] Butcher, K. S. A., Afifuddin, Chen, P. P. T. & Tansley, T. L. Studies of the plasma related oxygen contamination of gallium nitride grown by remote plasma enhanced chemical vapour deposition. physica status solidi (c) 156–160 (2002). doi:10.1002/pssc.200390012

[57] Lee, Y. J. & Kang, S.-W. Growth of aluminum nitride thin films prepared by plasma-enhanced atomic layer deposition. Thin Solid Films 446, 227–231 (2004).

[58] Ozgit-Akgun, C., Goldenberg, E., Okyay, A. K. & Biyikli, N. Hollow cathode plasma-assisted atomic layer deposition of crystalline aln, Gan and $Al_xGa_{1-x}N$ thin films at low temperatures. J. Mater. Chem. C 2, 2123–2136 (2014).

[59] Burns, J. C. et al. Introducing symmetric li-ion cells as a tool to study cell degradation mechanisms. Journal of The Electrochemical Society 158, (2011).

[60] Noguchi, Y., Kobayashi, E., Plashnitsa, L. S., Okada, S. & Yamaki, J.-ichi. Fabrication and performances of all solid-state symmetric sodium battery based on NASICON-related compounds. Electrochimica Acta 101, 59–65 (2013).

[61] Potentiostat Fundamentals. Potentiostat/Galvanostat Electrochemical Instrument Basics Available at: https://www.gamry.com/application-notes/instrumentation/potentiostat-fundamentals/.

[62] Stuve, E. M., Kreysa, G., Ota, K. I. & Savinell, R. F. in Encyclopedia of applied electrochemistry, Overpotentials in Electrochemical Cells (Springer, 2014).

[63] Stuve, E. M., Kreysa, G., Ota, K. I. & Savinell, R. F. in Encyclopedia of applied electrochemistry, Electrochemical Impedance Spectroscopy (EIS) Applications to Sensors and Diagnostics (Springer, 2014).

[64] Kozen, A. C. et al. Stabilization of lithium metal anodes by hybrid artificial solid electrolyte interphase. Chemistry of Materials 29, 6298–6307 (2017).

[65] Wang, Y. et al. Electrochemically controlled solid electrolyte interphase layers enable superior Li–S Batteries. ACS Applied Materials & Interfaces 10, 24554–24563 (2018).